Journal of Comparative Neurology

WILEY

JCN RESEARCH IN SYSTEMS NEUROSCIENCE THE JOURNAL OF COMPARATIVE NEUROLOGY

RESEARCH ARTICLE

Predictive Methods and Probabilistic Mapping of Subcortical Brain Components in Fossil Carnivora

Emily Baer[1] | Phuoc D. Nguyen[1] | Stefan Lilly[1] | Jiyoon Song[1] | Mathew Yee[1] | Olivia Matz[1] | Rachna Sahasrabudhe[1] | Douglas R. Hall[1] | Susan La[1] | Brandon J. Merritt[1] | Pallavi Mahesh[1] | Christelle Eliacin[1] | Kathleen Bitterman[1] | Demi Oddes[2] | Mads F. Bertelsen[3] | Cheuk Y. Tang[4] | Peter F. Cook[5] | Rogier B. Mars[6,7] | Patrick R. Hof[8,9] | Rachel Dunn[1] | Paul R. Manger[2] | Chet C. Sherwood[10] | Muhammad A. Spocter[1,2,11]

[1]Department of Anatomy, Des Moines University, West Des Moines, Iowa, USA | [2]School of Anatomical Sciences, Faculty of Health Sciences, University of the Witwatersrand, Johannesburg, Republic of South Africa | [3]Center for Zoo and Wild Animal Health, Copenhagen Zoo, Frederiksberg, Denmark | [4]Departments of Radiology and Psychiatry and BioMedical and Engineering Imaging Institute, Icahn School of Medicine at Mount Sinai, New York, New York, USA | [5]Florida Institute for Marine Mammal Sciences, New College of Florida, Sarasota, Florida, USA | [6]Wellcome Centre for Integrative Neuroimaging, FMRIB, Nuffield Department of Clinical Neurosciences, University of Oxford, Oxford, UK | [7]Donders Institute for Brain, Cognition and Behavior, Radboud University Nijmegen, Nijmegen, The Netherlands | [8]Nash Family Department of Neuroscience and Friedman Brain Institute, and Center for Discovery and Innovation, Icahn School of Medicine at Mount Sinai, New York, New York, USA | [9]New York Consortium in Evolutionary Primatology, New York, New York, USA | [10]Department of Anthropology and Center for the Advanced Study of Human Paleobiology, The George Washington University, Washington, District of Columbia, USA | [11]College of Veterinary Medicine, Department of Biomedical Sciences, Iowa State University, Ames, Iowa, USA

Correspondence: Muhammad A. Spocter (Muhammad.spocter@dmu.edu)

Received: 20 August 2024 | **Revised:** 28 November 2024 | **Accepted:** 30 December 2024

Funding: This work was supported by funding from the Iowa STEM BEST (MAS), and the Carnegie-Wits Alumni Diaspora Program through the Carnegie Corporation of New York (MAS and PRM). Data acquisition in Oxford was supported by the Biotechnology and Biological Sciences Research Council (BBSRC) UK [Grants BB/W019582/1]. The Wellcome Centre for Integrative Neuroimaging is supported by core funding from the Wellcome Trust [Grant 203139/Z/16/Z].

Keywords: brain | Carnivora | evolution | fossils | prediction | probabilistic | simulation

ABSTRACT

Paleoneurology reconstructs the evolutionary history of nervous systems through direct observations from the fossil record and comparative data from extant species. Although this approach can provide direct evidence of phylogenetic links among species, it is constrained by the availability and quality of data that can be gleaned from the fossil record. Here, we sought to translate brain component relationships in a sample of extant Carnivora to make inferences about brain structure in fossil species. Using high resolution magnetic resonance imaging on extant canids and felids and 3D laser scanning on fossil Carnivora, spanning some 40 million years of evolution, we derived measurements for select brain components. From these primary data, predictive equations of cortical (gray matter mass, cortical thickness, and gyrification index) and subcortical structures (caudate nucleus, putamen, and external globus pallidus mass) were used to derive estimates for select fossil Carnivora. We found that regression equations based on both extant and simulation samples provided moderate to high predictability of subcortical masses for fossil Carnivora. We also found that using exploratory probabilistic mapping of subcortical structures in extant Carnivora, a reasonable prediction could be made of the 3D subcortical morphospace of fossil endocasts. These results identify allometric departures and establish adult species ranges in brain component size for fossil species. The integrative approach taken in this study may serve as a model to promote further dialog between neurobiologists working on extant Carnivora models and paleoneurologists describing the nervous system of fossils from this understudied group of mammals.

Associate Editor: Pooja Balaram.

1 | Introduction

Brains do not fossilize, and aside from the rare examples of mummified remains (e.g., Kharlamova et al. 2015), the study of mammalian brains in an evolutionary context has relied mainly on two sources of primary data: (1) the study of brain structure and function in extant species; and (2) the study of endocranial casts (natural, artificial or virtual) in fossil taxa. Both of these approaches have their benefits and limitations. For example, although the study of brain structure in extant species has emerged as a powerful approach for directly evaluating species differences in cortical and subcortical brain structure, function, and molecular biology (e.g., Foubet et al. 2024; Racicot et al. 2024; Boch et al. 2024; Oddes et al. 2023; Sacco et al. 2023; Nguyen et al. 2020), this approach can only allow for inferences to be made about the past based on assumptions concerning patterns of evolution (Mitchell 2015; Slater, Harmon, and Alfaro 2012). In contrast, although the study of endocast morphology in fossil taxa represents direct evidence of the external anatomy of brains in extinct species from the past, this approach is limited by the paucity and quality of available data extracted from the endocast, thus constraining paleoneurological study to comparisons of surface anatomy and external brain volumetry (Labra et al. 2024; Domoncel et al. 2021; Borne et al. 2020; Beaudet and Gilissen 2018; Jerison 2012). Given these limitations, a productive approach is to integrate their combined strengths to expand the scope of available paleoneurological study and prediction.

Although there is generally a close association between the meningeal surface of the brain and the overlying endocranium, this relationship (i.e., the residual space) is not uniform across all orders (Mettler 1956; Blinkov and Glezer 1968; Tobias 1994) as is evident in the comparative endocast morphology of primates where the residual space and accompanying meninges obscure the impression of the cortical surface (Bruner, Ogihara, and Tanabe 2018). In this regard, study of the Carnivora represents a promising opportunity for merging these complementary lines of evidence as the topography of the brain can be more readily extracted from endocasts (Radinsky 1973, 1975; Lyras 2009). In addition, recent studies of brain anatomy and volumetrics in extant Carnivora have provided high quality, spatially-relevant quantitative data on the relationship between the brain surface and its subcortical structures (e.g., Foster et al. 2024; Nelson et al. 2024; Grewal et al. 2020; Chengetania et al. 2020; Spocter et al. 2018).

The order Carnivora is composed of over 290 extant species arranged into two major suborders, the canids and the felids (Hassanin et al. 2021). Studies on the evolutionary history of this group have traced the oldest known Carnivora fossils to the late Paleocene (Spaulding and Flynn 2012; Solé et al. 2016); however, the taxonomy and evolutionary history of this group still remain a subject of ongoing debate (Law, Slater, and Mehta 2018). One of the major difficulties in reconstructing the evolutionary history of this group is that carnivores are relatively scarce in the ecological landscape. This sparse distribution manifests in the fossil record as small sample sizes which are further complicated by preservation differences resulting from taphonomic processes.

To date, paleoneurological studies of the Carnivora have relied largely on endocranial volume measurements (e.g., Michaud, Toussaint, and Gilissen 2022; Sakai et al. 2016; Finarelli and Flynn 2009) to compare scaling analyses of the whole brain or external components to body size (Sakai et al. 2011; Lyras et al. 2016). As a complementary line of investigation, studies in extant species have long demonstrated that such scaling analyses (using both traditional and phylogenetic regression approaches) can be used with a high degree of reliability to predict the scaling relationship between brain components (e.g., Smaers et al. 2021; Yopak et al. 2010; Bush and Allman 2004; Spocter and Manger 2007) and that such consistencies are indicative of the underlying constraints (i.e., energetic, developmental, and phylogenetic) of these biological systems (e.g., Manger, Spocter & Patzke, 2014; Finlay and Darlington 1995; Finlay, Darlington, and Nicastro 2001). Given the robustness of these techniques, these approaches have tremendous potential to predict brain component size and shape in the fossil Carnivora. The ability to make such predictions in fossil Carnivora would widen the scope of available data and improve our ability to reconstruct the evolutionary history of nervous systems in Carnivorans.

With this goal in mind, we investigated the scaling relationships of select cortical and subcortical brain components in the Carnivora and used a combination of phylogenetically informed regression analyses as well as simulation studies to generate robust predicative equations of the gray matter (GM), caudate (including nucleus accumbens), putamen, external globus pallidus, and striatal mass, as well as cortical thickness (CT) and gyrification index (GI) for select fossil Carnivora. The use of these predictive equations and resulting estimates of brain component size may allow researchers to better infer the biology and behavior of fossil Carnivora. In addition, the resulting confidence intervals and ranges derived from this study would help inform researchers looking to identify departures from allometry and establish adult species ranges in brain and brain component size for fossil taxa.

2 | Materials and Methods

Our imaging dataset comprised two primary sources, (1) structural scan data obtained from magnetic resonance imaging (MRI) of post-mortem brains of extant Carnivora; and (2) surface morphology data obtained through laser scanning of fossil carnivore endocasts.

2.1 | Extant Carnivora Specimens

This dataset consists of MRI of post-mortem brains obtained from 12 extant Carnivora species. The dataset included six wild canid species (*Canis lupus lupus* $N = 1$ adult male; *Canis latrans* $N = 1$ adult female; *Speothos venaticus* $N = 1$ adult male; *Chrysocyon brachyurus* $N = 1$ adult male; *Lycaon pictus* $N = 1$, adult male; *Vulpes vulpes* $N = 1$, adult male; *Vulpes zerda* $N = 1$, adult male), three wild felid species (*Panthera uncia*, $N = 1$, male 6-years-old; *Panthera tigris altaica* $N = 1$, female 12-years-old; *Panthera tigris tigris* $N = 1$, female Adult), two domestic canids (*C. lupus familiaris,* $N = 2$, male 9-months old; female 2-years-old), and one domestic felid *(Felis silvestris cattus* $N = 1$, adult female). A complete species list is included in Table 1, and their phylogenetic relationship to one another is shown in Figure 1a,b.

TABLE 1 | Species list and associated brain and basal nuclei mass in grams (g).

Species	Brain mass (g)	Caudate mass (g)	Putamen mass (g)	Pallidal mass (g)	Striatal mass (g)	Basal nuclei mass (g)
Felis catus (FC1)	25.39	0.43	0.08	0.03	0.51	0.54
Panthera uncia (PU)	69.09	1.02	0.15	0.10	1.17	1.27
Panthera tigris altaica (PT1)	231.24	2.57	0.34	0.18	2.90	3.08
Panthera tigris tigris (PT2)	220.02	1.07	0.34	0.21	1.41	1.62
Canis latrans (CL1)	75.34	1.21	0.27	0.07	1.48	1.55
Canis lupus (CL1)	139.76	2.08	0.27	0.24	2.35	2.59
Lycaon pictus (LP1)	132.82	1.75	0.36	0.15	2.10	2.25
Vulpes zerda (VZ1)	16.27	0.34	0.03	0.03	0.37	0.40
Vulpes vulpes (VV1)	45.15	0.83	0.09	0.08	0.92	1.01
Speothos venaticus (SV)	43.53	0.93	0.04	—	0.98	—
Chrysocyon brachyurus (CB2)	91.29	1.35	0.16	0.17	1.50	1.67
Canis lupus familiaris (D1)	61.30	1.08	0.12	0.07	1.20	1.27
Canis lupus familiaris (D2)	75.09	1.38	0.23	0.11	1.60	1.71

Note: Volumes were converted to mass through use of the specific gravity of brain tissue (1.036 g/cm^3; Stephan 1960). The subcortical masses are the summed bilateral mass for each of the basal nuclei components. Note striatal mass was calculated by summing putamen mass and caudate (head, body and tail) mass.

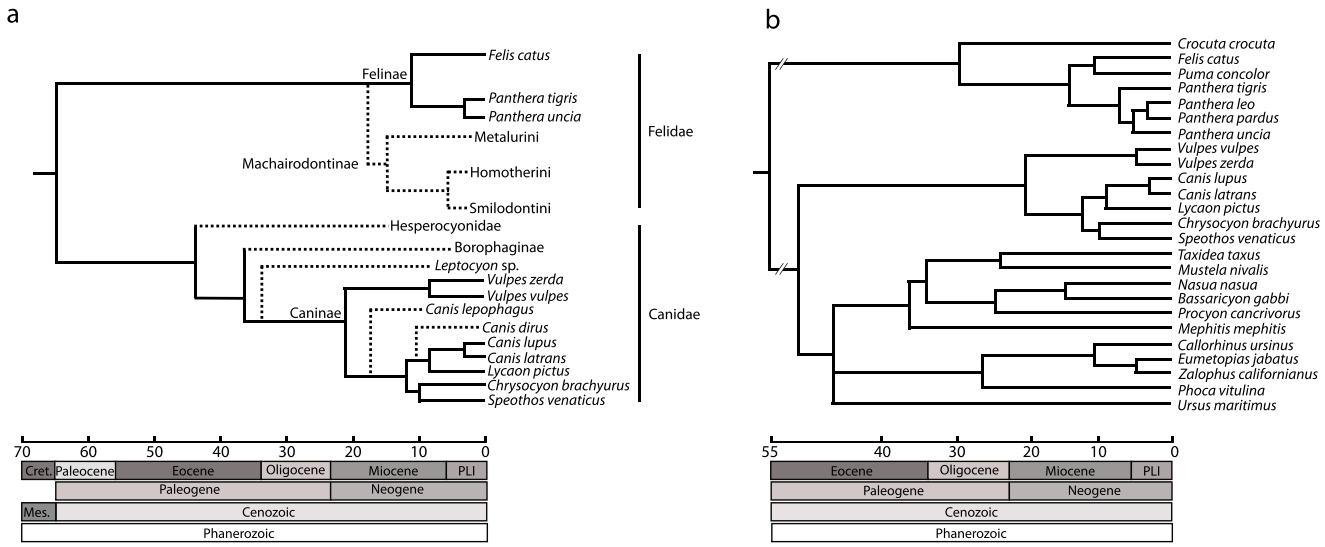

FIGURE 1 | (a) A composite phylogeny showing the phylogenetic relationship of the fossil taxa included in this study to the extant Carnivora used for phylogenetic analysis. The phylogeny was derived using Hassanin et al. (2021), Perri et al. (2021), Tedford et al. (2009), Werdelin et al. 2010, Lyras (2009), and Radinsky (1973, 1975); (b) Phylogeny used in the implementation of phylogenetic generalized least squares (PGLS). PGLS was performed used the caper package (Orme et al. 2018). The phylogeny was constructed using data based on the mammalian super-tree (Nyakatura and Bininda-Edmonds 2012) as well as reference to the open source resource TimeTree.org.

2.2 | Fossil Carnivora Specimens

This dataset consists of surface morphology data obtained through laser scanning of eight fossil endocast specimens obtained on loan from the Field Museum in Chicago to Des Moines University Department of Anatomy (Table 2). The phylogenetic relationship of these fossil Carnivora is presented in Figure 1a. Several of these endocasts were created by Leonard Radinsky during original delineation of radiation patterns (Radinsky 1973). Below is a brief description of endocast quality and preservation, making particular reference to accession numbers found in Table 2. Representative images of the fossil endocasts are also shown in Figure 2. PM394—*Canis dirus. Note that in recent publications C. dirus is also reffered to as Aenocyon dirus* (e.g., Perri et al. 2021)—well preserved endocasts with intact cerebral blood vessels and meninges. Missing frontal portions of olfactory bulb bilaterally. Has an orthogonal shaped coronal sulci outline. PM58951—*Aelurodon ferox*—a description of morphology was recorded by Radinsky (1973). PM58953—*Canis lepophagus*—complete endocast with limited relief of sulci across the cerebral cortex. Observable orthogonal cortex medial to the coronal sulci, difficult to determine size

TABLE 2 | Details of the fossil Carnivora endocasts digitized in the current study.

Accession Number	Taxon	Taxonomic Group.	Estimated ECV (cm^3)	Brain mass (g)
PM58861	*Homotherium*	Metailurinae	252.73	261.83
PM58862	*Metailurus*	Metailurini	102.72	106.42
PM58868	*Ischyrosmilus*	Homotherini	194.80	201.82
PM58870	*Pseudaelurus*	Felinae	72.15	74.75
PM58872	*Proailurus*	Felinae	44.10	45.69
PM58951	*Aelurodon* sp.	Borophaginae	116.96	121.17
PM58953	*Canis lepophagus*	Caninae	46.22	47.88
PM394	*Canis dirus*	Caninae	163.76	169.65
PM58963	*Borophagus*	Borophaginae	187.39	194.14
PM58961	*Leptocyon* sp.	Caninae	14.50	15.02

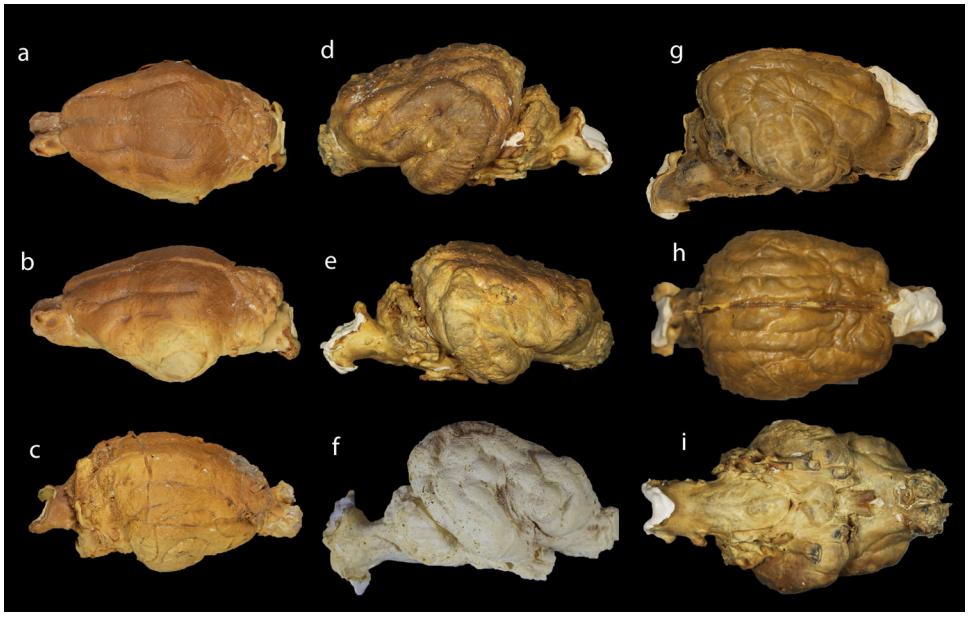

FIGURE 2 | Representative images of the fossil Carnivora endocasts used in the current study. Parts (a and b) are superior and lateral views of the *Leptocyon* sp. (PM58961); part (c) is a lateral view of the *Aelurodon* sp. (PM58951); parts (d and e) are lateral views of *Borophagus dudleyi* (PM58963); part (f) a lateral view of *Homotherium* sp. (PM58661); parts (g–i) are lateral, superior, and inferior views of *Canis dirus* (dire wolf -PM394).

of the proreal gyrus. PM58961—*Leptocyon sp*—complete endocast with description by Radinsky (1973). PM58963—*Borophagus dudleyi*—complete endocast with intact cerebral blood vessels and meninges. A description of morphology was recorded by Radinsky (1973). PM58977—*Phlaocyon marslandensis*—slightly damaged endocast with poorly preserved ventral and caudal aspects. A description of morphology can be found recorded by Radinsky (1973), and Lyras (2009). PM58990—*Canis edwardii*—well preserved endocasts with damage to the left caudal portions of the cerebral hemisphere, and bilateral damage to the ventral cerebrum. Proreal gyrus is well developed, and coronal sulci form an orthogonal outline. PM59036- *Enhydrocyon stenocephalus*—a description of morphology can be found recorded by Radinsky (1973) and Lyras (2009).

2.3 | Imaging

2.3.1 | Structural MRI Acquisition and Processing in Extant Carnivora

MRI was performed on the whole brains of 13 carnivore species. Whole brain and caudate nucleus volume data were obtained through segmentation procedures. All scanning was carried out in strict accordance with the recommendations in the Guide for the Care and Use of Laboratory Animals of the National Institutes of Health and approved by the Institutional Animal Care and Use Committees of Des Moines University, as well as the Animal Ethics and Screening Committee (AESC) of the University of the Witwatersrand (AESC No. 2012/53/01). MR

images were obtained from two imaging facilities: the Department of Diagnostic, Molecular, and Interventional Radiology, Icahn School of Medicine at Mount Sinai; and the Department of Radiology at Oxford University. The brains of specimens FC1, PU, PT1, PT2, VV1, VZ1, LP1, CB2, D1, and D2 were scanned at the Icahn School of Medicine using a 7T Bruker Biospec MR System. Specimens were removed within 14 h of death and immersion fixed in 10% formalin at necropsy before being transferred to a solution of 0.1 M phosphate buffered saline (PBS) with 0.1% sodium azide solution and stored at 4°C prior to scanning. A 3D FLASH sequence was used with the following parameter settings: TR (time to repetition) = 36 ms, TE (time to echo) = 23 ms, flip angle = 15°, FOV (field of view) = 128 × 128 × 175 mm^3, matrix size = 384 × 384 × 384 mm^3 in each slab, 20 averages, slice thickness = 0.5 mm, and 3D isotropic resolution of 0.30 mm. Scanning performed at Oxford University was performed using a 7 T Bruker Biospec MR System. Following overdose with sodium pentobarbital (200 mg/kg, i.v.) the heads of animal CL1 and SV were perfusion-fixed within 15 min after death in 4% paraformaldehyde in 0.1 M phosphate buffer (PB) before being postfixed in 4% paraformaldehyde in 0.1 M PB for 48 h before and placed into storage. Scanning was performed at the Wellcome Centre for Integrative Neuroimaging, Nuffield Department of Clinical Neurosciences, University of Oxford. The specimens were scanned on a Siemens 7 T whole-body scanner (28ch-receive/1ch-transmitl knee coil—QED). For specimen CL1, a high-resolution structural scan was acquired using a true fast imaging with steady-state free-precession (TRUFI) sequence, TR = 14.65 ms, TE = 7.33 ms, flip angle = 30°, FOV = 118 × 160 × 99 mm^3 in each slab, matrix size = 542 × 736 × 448 mm^3, and 3D isotropic resolution of 0.22 mm. For specimen SV, a 2D diffusion-weighted spin-echo multi-slice protocol with single line readout (DW-SEMS; TR/TE = 19/26 ms; matrix size = 128 × 128) with a sufficient number of slices to cover each brain was used to create 0.6 mm isotropic data. A ball and stick model (Behrens et al. 2007, MRM) was used to preprocess the data from which a T1-contrast image was created (cf. Boch et al. 2024).

Following MR image acquisition, the datafiles were loaded into Analyze software version 10.0 (www.analyzedirect.com) for postprocessing. The postprocessing steps involved resectioning the image sequences along the A-P plane to facilitate import into ITKSNAP software (http://www.itksnap.org). MR images were loaded into ITKSNAP for subcortical segmentation and surface reconstruction. The ITKSNAP toolkit provides several options for both automatic segmentation (using Region Competition Snakes and Geodesic Active contours) as well as fully manual segmentation procedures (Yushkevich et al. 2006). We used manual segmentation procedures to isolate and reconstruct the basal nuclei components. Using the region of interest tool, the putamen, external globus pallidus, and caudate nucleus were outlined in coronal slices. Segmentation outlines were completed by EB, PDN, SL, JS, OM, and DAH and visually inspected by MAS for consistency between investigators and with close reference to the relevant anatomical atlases on Carnivora and human brains (e.g., Palazzi 2011; Mai et al. 2015). Interobserver congruency was assessed in a pilot study using Lin's concordance correlation coefficient. Despite some interobserver variability in the caudal delineations of the nuclei, our pilot study indicated that the delineations were highly reproducible between observers (i.e., Lin's coefficient 85%–90%). Segmentations of the caudate nucleus included reconstructions of the head, body and tail portions with accompanying volumes recently reported by our group (Foster et al. 2024). We recognize that the corpus striatum is composed of the dorsal and ventral striatopallidal (SP) complexes, with the dorsal SP complex including the caudate and putamen, while the ventral SP includes the nucleus accumbens, substantia innominate, and olfactory tubercle. For pragmatic reasons, where possible, we quantified subcomponents of the corpus striatum separately. Because of difficulties adequately separating the ventral striatum (nucleus accumbens) from the merged putamen and caudate nucleus anteriorly, our definition of the caudate nucleus pragmatically includes the nucleus accumbens to the exclusion of the putamen. Our definition of the striatum includes the caudate nucleus, putamen and nucleus accumbens. For convenience, our definition of the basal nuclei includes the caudate nucleus, putamen, nucleus accumbens and external globus pallidus.

Representative images showing the parcellation and segmentation procedure for the basal nuclei are provided in Figure 3. Segmentations of the cortical grey matter surface and subsequent calculation of the GI, formed part of an earlier study by our group (Grewal et al. 2020). In brief, processing of the resultant MR images was performed in BrainVisa ((http://brainvisa.info/web/index.html, RRID:SCR_007354) using the Morphologists pipeline. MR images were loaded into Morphologist pipeline and processed to create 3D white matter and pial surface reconstructions, which were then exported to MeshLab (http://www.meshlab.net/, RRID:SCR_003430) where the GI was calculated as the ratio of the surface area of the pial surface area to the area of the convex hull (Rogers et al. 2010). Associated whole brain volumes were also segmented for each specimen using semi-automatic segmentation. For a complete methodological outline as it applies to the study of Carnivora gyrification, we direct the reader to Grewal et al. (2020). The final 3D reconstructions were then saved as stereolithographic files before being imported into MeshLab (http://www.meshlab.net/) where volumes were computed for each mesh and tabulated in Microsoft Excel in preparation for statistical analyses.

2.3.2 | Laser Scanning Acquisition and Processing in Fossil Carnivora

Laser scanning of fossil endocasts was undertaken using a NextEngine 3D ULTRA HD laser scanning imaging system. This desktop scanner is known for its ease of use and accuracy for extracting surface geometries and 3D mesh data (Slizewski et al. 2010). During processing each endocast was placed on the accompanying scanner turntable/pedestal which permitted 360° scanning of each specimen, using the accompanying ScanStudio software. The distance between the laser scanner and the endocast was measured to determine if the macro or wide setting would be utilized. Note was taken to ensure that the entire specimen was within the scanning zone of the laser. Eleven divisions of each endocast angle were recorded, and the target setting adjusted based on the coloration. Each endocast was scanned at the initial angle and then again after a 90° rotation. Scans were then trimmed and scanning divisions compressed in ScanStudio to generate a 3-D virtual model showing two separate angles of each endocast (Figure 4). The compressed

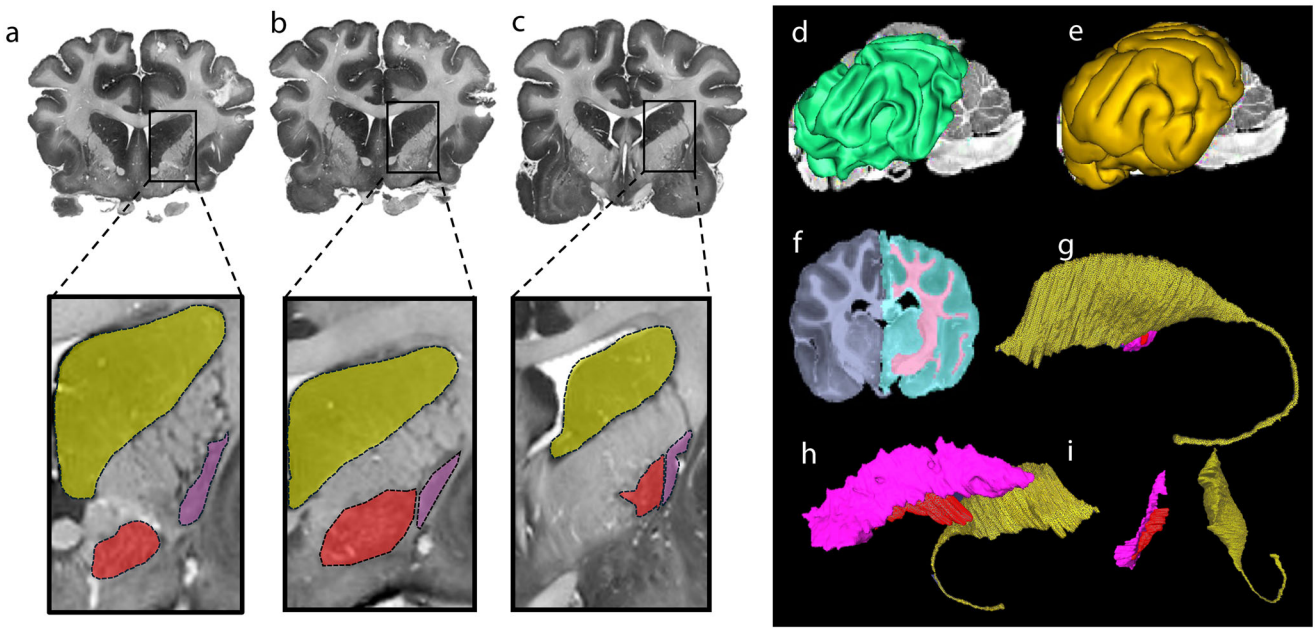

FIGURE 3 | (a–c) Representative MR coronal images through the diencephalon of a canid (*Canis lupus domesticus*); showing the manual segmentation of the caudate nucleus, external globus pallidus and putamen; (d–f) screenshots of the gray and white matter reconstructions used for calculating the Gyrification Index (GI) as described in Grewal et al. (2020); (g–i) representative screenshots of completed 3D surface reconstructions of the caudate nucleus, putamen and external globus pallidus as obtained from manual segmentation in ITKSNAP.

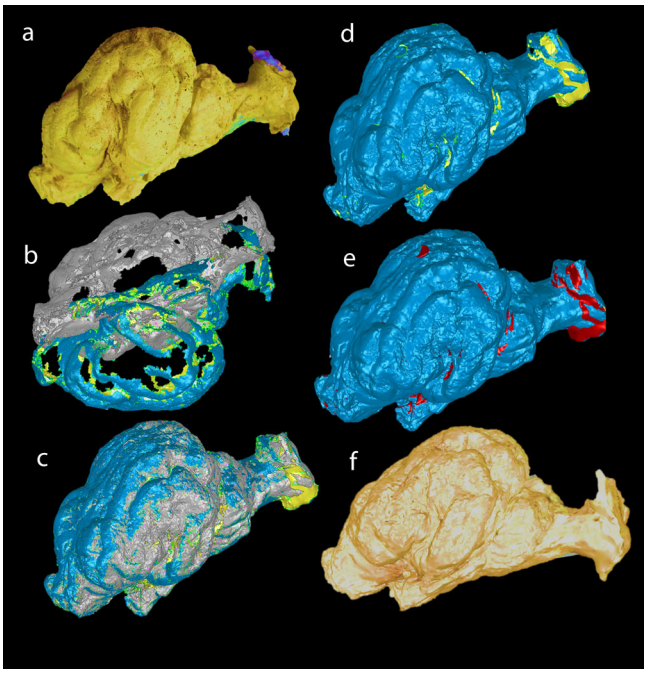

FIGURE 4 | Images showing the processing of a fossil endocast (*Homotherium* sp. PM58861). Laser scanning was undertaken using the NextEngine 3D ULTRA HD laser scanning system. (a) A lateral image of the endocast prior to be placed on was placed on the scanner pedestal; (b) an image of the resulting scans in ScanStudio. Scans trimmed and scanning divisions compressed in ScanStudio to generate a 3-D virtual model showing two separate angles of each endocast; (c) The compressed spatial object of the endocast prior to be being imported into GEOMAGIC for postprocessing; (d–f) a sequence of screenshots of the post-processed 3D scan undergoing noise and polygon reduction, filling and alignment.

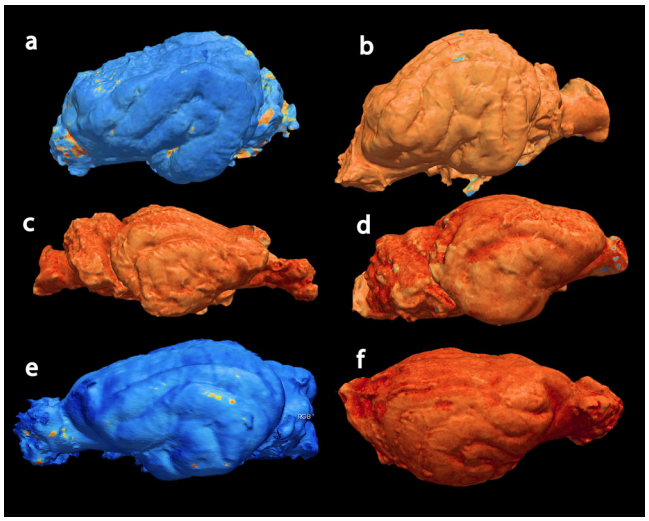

FIGURE 5 | Representative 3D reconstructions of the final virtual endocasts derived from processing in Geomagic. (a) Lateral views of the domestic dog brain for comparison with the fossil endocasts; (b) endocast of PM58862; (c) is a lateral view of PM58870; (d) lateral view of *Proailurus lemanensis* (PM58872); (e) a lateral view of *Phlaocyon marslandensis* (PM58977); (f) superior lateral view of the *Canis edwardii* (PM58990).

spatial object of the endocast was then imported into GEOMAGIC for postprocessing (i.e., noise and polygon reduction, filling, and alignment) before the final 3D reconstruction was saved as a stereolithographic file that was imported into MeshLab to compute the endocast volume for each specimen. Total scan time for each specimen was approximately 2 h with an additional hour of post-scan processing. Representative 3D reconstructions of the final virtual endocasts are shown in Figure 5.

2.4 | Data Analysis

2.4.1 | Putamen:Caudate, Pallidal:Caudate, and Pallidal:Putamen Ratios

To evaluate the consistency in subcortical proportions between extant Carnivora, we calculated the basal nuclei ratios (i.e., pallidal:putamen ratio; putamen:caudate ratio) and visually evaluated these for any deviations amongst the Carnivora.

2.4.2 | Predictions Based on Regression Analyses on Extant Data

In addition, we used a combination of phylogenetic generalized least squares (PGLS) regression analysis and simulation studies to evaluate the scaling relationships of the cortical and subcortical components against brain mass. All statistical analyses were undertaken in R Version 3.4.1 (www.r-project.org/. PGLS was performed using the "caper" package (Orme et al. 2018). The phylogeny used in the current study is shown in Figure 1b as derived from (Bininda-Emonds et al. 2007; Nyakatura and Bininda Emonds 2012). All volumetric measures were converted to mass using the specific mass of brain tissue, by multiplying the volume by a factor of 1.036 g/cm^3 (Stephan 1960, 1981; Rehkamper et al. 1991). Before inclusion in statistical analyses, all data were log-transformed (base 10). In cases where multiple scans were available for a species, the average was calculated and included as a single datapoint in subsequent regression analyses. Confidence and prediction intervals were calculated using the EvoMaps add-on package (Smaers, Mongle, and Kandler 2016), whereas slope and intercept comparisons were undertaken using SMATR Version 3 (Warton et al. 2011). The raw data used to derive these relationships are shown in Tables 1 and 2. Resulting regression equations based on the extant Carnivora were then used to predict the mass of cortical and subcortical brain components for the fossil species. Endocranial volumes for fossil Carnivora (computed in Section 2.3.2) were combined with published estimates collated from the literature and converted to mass (g) before being entered into the regression equations. Given the known transformation bias that occurs when using logarithmic transformation followed by detransformation (Smith 1993), we also computed the smearing estimator for select equations. This estimator was multiplied with the detransformed values to provide a final estimate of the brain components in each fossil species.

2.4.3 | Predictions Based on Regression Analyses on Simulation Data (SIM)

Because our resultant regression statistics were based on a small number of extant species, we undertook an exploratory step to determine if generating a simulated dataset would improve our regression analyses and predictive ability. We generated a simulated dataset of $N = 100$ individuals, using the variance–covariance structure observed in our extant sample. The simulated dataset was generated in R using the MASS library (mvtnorm). Once generated, least squares regression analysis was applied to the log-transformed simulated dataset, and a new set of predictive equations and smearing estimators was calculated and used to predict brain component size from endocranial volumes obtained for fossil taxa.

To test the utility of the predictive equations, we calculated endocranial volumes for our sample of virtual fossil endocasts and combined these data with published endocranial volumes for select fossil Carnivora. Endocranial volumes for the fossil taxa were converted to mass (g) (Stephan 1960) and log-transformed (base 10) prior to inclusion in the regression equations. Brain component size was then estimated using equations derived from both the extant and simulation samples and then assessed based on their comparative regression statistics, error ranges, and the limits of agreement using Bland–Altman plots created in BA-plotteR (Goedhart and Rishniw 2021).

2.5 | Probabilistic Mapping of Subcortical Anatomy in Fossils

As an exploratory step, we created visualizations of the predicted volumes of the striatum and white matter for a single fossil specimen, *C. dirus* (PM394- dire wolf) to serve as a model for further development of these techniques. Comparative mesh data for the caudate nucleus of eight extant Carnivora were aligned in CloudCompare using the point alignment tool. This tool aligns entities by making use of user defined point registration between a reference (R) and target (A) entity. Starting with the coyote caudate nucleus, three reference point pairs were identified on each species mesh (i.e., R0—the anterior most projecting point on the head of the caudate nucleus; R1—the most superior projecting point on the head of the caudate nucleus; and R2—the most lateral projecting point on medial aspect of the caudate body) before alignment, with scale adjustment to match the size of the reference coyote mesh (Figure 6a–c). The transformation matrix was saved and applied sequentially to each remaining mesh. Once alignment to the coyote mesh was completed, the dataset of meshes was spatially normalized using the Multiply/Scale function in CloudCompare to match the scale of PM394. The scale used for spatial normalization to PM394 was derived from the ratio of the whole brain mesh volumes (i.e., *C. latrans: C. dirus*; 75.33/169.65 = 0.44); therefore, the scale factor by which the overlapping meshes was adjusted was 1.44. The resultant probabilistic map of the caudate nucleus (see Figure 6e–h) was then exported to MeshLab to create a single merged mesh that consisted only of the overlapping areas of the original meshes. To remove non overlapping areas in the meshes, we used the Intersection Boolean operation enclosed within the Mesh layer Filter of MeshLab. This filter performs an exact Boolean intersection between each mesh (Zhou et al. 2016). Mesh files were processed in pairs with the coyote mesh serving as the reference mesh, whereas the new species mesh was the target mesh. Once the series of intersecting meshes was derived, the Union Boolean operation was performed to merge the meshes into a single mesh.

Similarly, a white matter probabilistic point cloud was also constructed using CloudCompare and MeshLab. The reference points used for mesh alignment are shown in Figure 7 and include three points on the sylvian sulcus (anterior, mid, and posterior) and a fourth point on the antero-medial surface of the cruciate sulcus (Figure 7a–c). The dataset of aligned white matter meshes

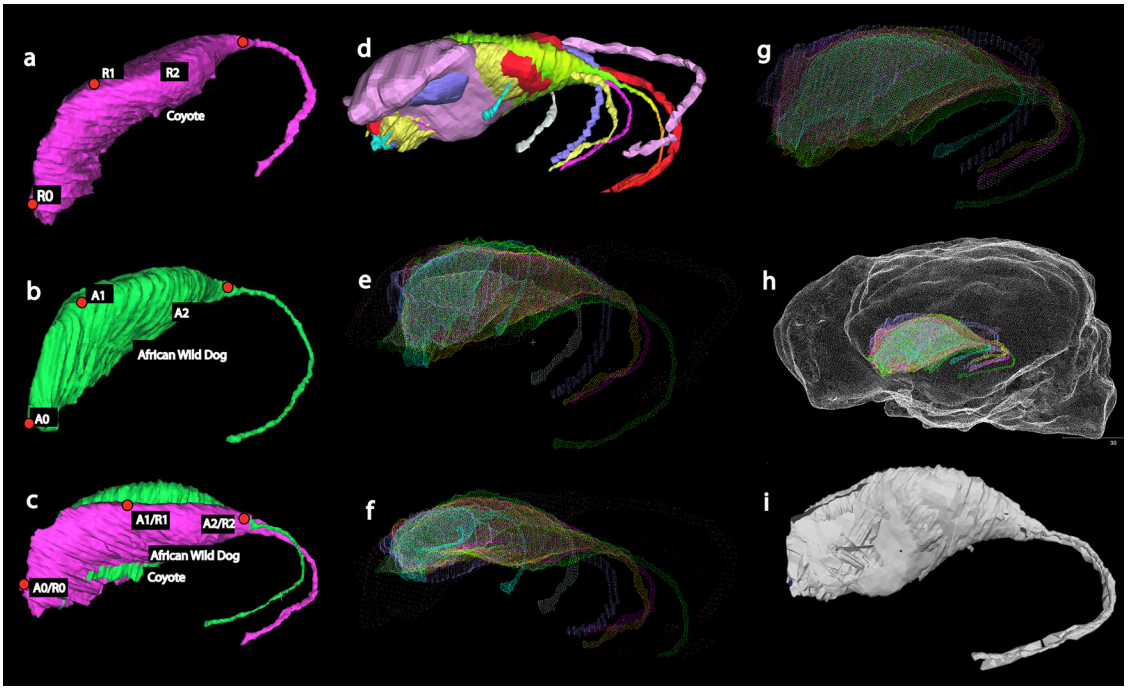

FIGURE 6 | (a–i) Representative images showing the alignment (point to point registration) and transformation of the caudate reconstructions as undertaken in CloudCompare. Reference and target landmarks are shown in (a–c); (d–g) shows the raw and transformed caudate species meshes and point clouds overlaid on one another; (h) shows the caudate overlays placed into the 3D point cloud of PM394; (i) shows the final Boolean intersected caudate mesh.

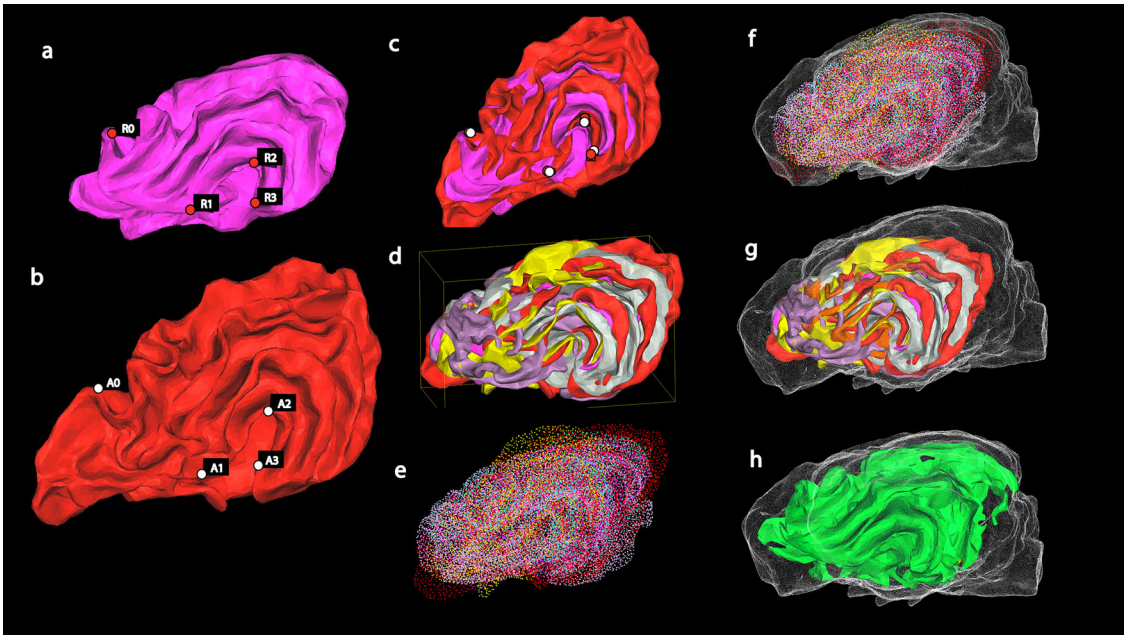

FIGURE 7 | (a–h) Representative images showing the alignment (point to point registration) and transformation of the white matter reconstructions as undertaken in CloudCompare. Reference and target landmarks are shown in (a–c); (d–g) shows the aligned and transformed white matter species meshes and point clouds overlaid on one another; (h) shows the white matter overlay derived from Boolean intersection placed into the 3D point cloud of PM394.

was spatially normalized using the Multiply/Scale function in CloudCompare to match the scale of PM394 (adjusted by scale factor 1.44 as derived from the coyote: PM394 brain volume ratio). The resultant white matter probabilistic map (see Figure 7d–g) was then merged into a single mesh using a combination of Boolean operations as described for the caudate nucleus (see above) (Figure 7h).

To determine the percentage overlap between the caudate meshes, we calculated the volumes of the intersecting mesh pairs

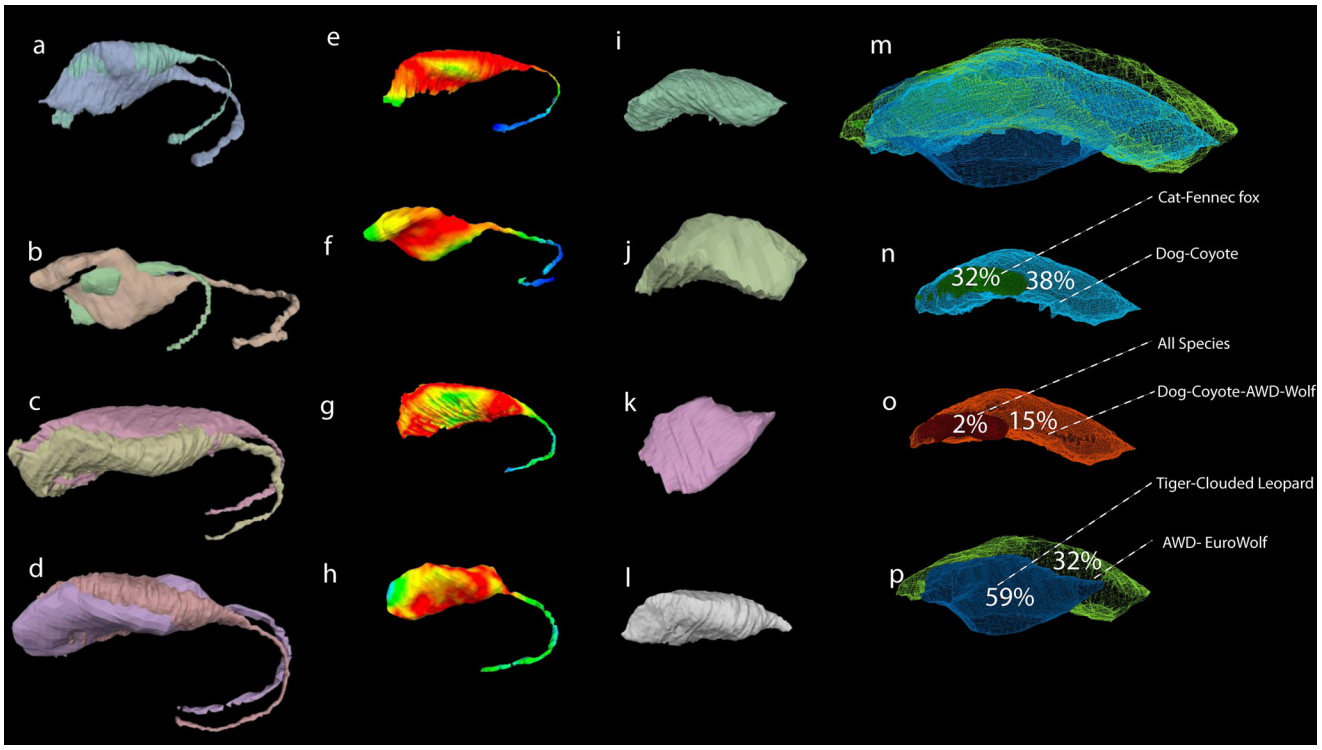

FIGURE 8 | (a–d) Representative images showing mesh pair alignment as completed in MeshLab and computation of the percentage overlap between caudate meshes; (e–h) Shows the resultant Hausdorff distances calculated for each mesh pairs with distances represented as a heat map (i.e., cool colors represent greater distanced between meshes, warmer colors are regions of the meshe that are closer to one another in overlap. Hausdorff distances were mapped back on to the vertex quality of the sample mesh for visualization; (i–l) shows the isolated Boolean intersecting volumes for each mesh pair; (m–p) shows the percentage overlap between the aligned and transformed mesh regions. Percentage overlap was obtained through Boolean operation by dividing the intersecting volumes by the total volume of the summed components and multiplying this value by 100. The total intersecting volume for the caudate was derived from the combination of intersecting mesh pairs and expressed as a percentage of total mesh volume.

obtained through Boolean operation by dividing the intersecting volumes by the total volume of the summed components and multiplying this value by 100. In addition, to facilitate visualization of overlapping caudate mesh pairs, we calculated the Hausdorff distance and mapped these distances on the vertex quality of the sample mesh as a heatmap. The total intersecting volume for the caudate was derived from the combination of intersecting mesh pairs and expressed as a percentage of total mesh volume (see Figure 8). Similarly, we determined the percentage overlap between the white matter meshes (left hemisphere only), using intersecting mesh pairs obtained through Boolean operation and dividing the intersecting volumes by the total volume of the summed components. In the case of the white matter meshes derived through Boolean operation (Intersection), repairs had to be made to the resultant meshes to make them airtight for volume estimation. Repairs were completed in MeshLab. Normals were checked to ensure that these pointed outward, and any holes were closed using the Remeshing, Simplification, and Reconstruction Filter. As a final step, a convex hull was created for each intersecting mesh to allow for immediate approximation of the volume enclosing the mesh surface (see Figure 9).

The final merged white matter and caudate mesh, representing the predicted subcortical structural space for PM394, was then merged with the endocast point cloud for PM394. Screenshots of the 3D models were also aligned and superimposed onto 2D images of the fossil endocast to facilitate visualization (see Figures 10 and 11).

3 | Results

3.1 | Putamen:Caudate, Pallidal:Caudate, and Pallidal:Putamen Ratios

To evaluate the proportional consistency in a select set of subcortical structures between the extant Carnivora, we calculated the pallidal:putamen and putamen:caudate ratios and evaluated these for any marked deviations amongst the species (see Figure 12 and Table 1). Amongst the canids, the coyote (*C. latrans*) had the largest putamen:caudate ratio (21%), followed by the African Wild dog, domestic dog (16%), European wolf (13%), maned wolf (11%), red fox (10%), and fennec fox (8%). Amongst the canids, the pallidal:caudate ratio appeared to be rather consistent and ranging within a narrow band (i.e., 6%–12%), with the largest ratio observed in the European wolf and maned wolves (12%), followed closely by that of the red fox (10%), the African Wild dog (8%), domestic dog (6%–8%), fennec fox (8%), and coyote (6%).

In the felids, the putamen:caudate ratio was largest in the snow leopard (31%), followed by the domestic cat (18%) and tiger (13%–15%). Amongst the felids, the pallidal:caudate ratio was largest in

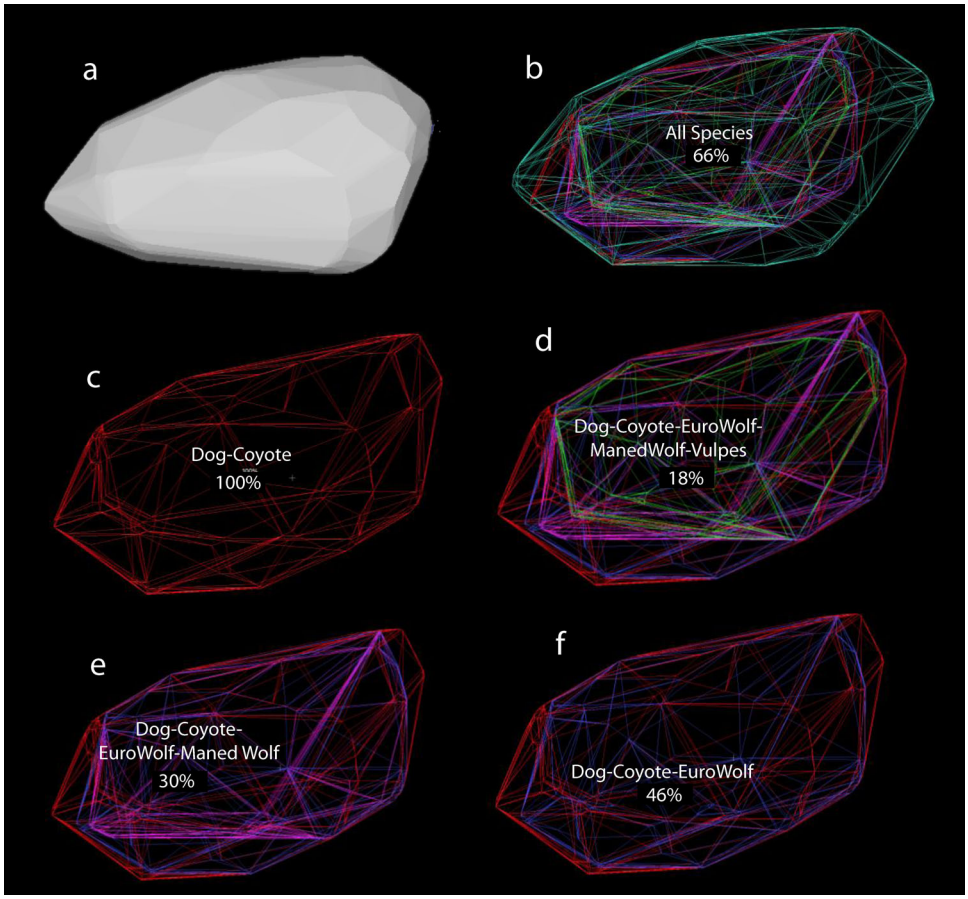

FIGURE 9 | (a–f) Representative images showing the percentage overlap between the white matter meshes as derived from the intersecting mesh pairs (Boolean Intersection). (a) Repairs were to the mesh were performed in MeshLab to make them airtight and a convex hull was created for each intersecting mesh to allow for immediate approximation of the volume enclosing the mesh surface; (b) shows the percentage overlap between white matter convex hulls for all species (c) shows the percentage overlap between the dog and coyote convex hull; (d) shows the percentage overlap between the dog, coyote, maned wolf and red fox convex hull; (e) shows the percentage overlap between the dog, coyote, maned wolf and European wolf convex hulls; (f) shows the percentage overlap between the dog, coyote, and European wolf convex hulls.

the snow leopard (20%) but ranged within a narrow band amongst the remaining felids (7%–10%). Across the Carnivora, putamen: caudate ratios averaged 15.5%, whereas the pallidal:caudate ratio averaged 9.5%.

3.2 | Predictions Based on Regression Analyses on Extant Data

To evaluate the scaling attributes of cortical and subcortical components against brain mass, we used PGLS regression analysis. A summary of the regression statistics derived from these analyses is shown in Table 3 and Figures 13 and 14. Brain mass is strongly correlated with the basal nuclei subcomponents across the Carnivora, with brain mass explaining 94%, 93%, 85%, and 79% of the variation in caudate nucleus, striatum, external globus pallidus, and putamen, respectively. When scaling analyses of striatal mass in the extant felids and canids are compared with that of other terrestrial Carnivora collated from the literature (see Reep, Finlay, and Darlington 2007), we once more observe a strong predictive relationship with brain mass, such that 93% of the variation in striatal mass across mammals is explained by brain mass (Table 3, Figure 14a,b). Although the regression statistics varied between the three mammalian groups (i.e., felid slope = 0.73; intercept = −1.20; r^2 = 0.63; canid slope = 0.73; intercept = −1.24; r^2 = 0.89; terrestrial mammal slope = 0.87; intercept = −1.27; r^2 = 0.96), statistical testing using analysis of covariance revealed that there was no significant difference between the three regression slopes and intercepts and that a common slope could be drawn for all the species (common mammalian slope = 0.84; lower = CI 0.72, upper CI = 0.97). However, when the regression statistics for the terrestrial Carnivora are compared with that of the aquatic Carnivora (Aquatic Carnivora slope = 0.47; intercept = −0.32; r^2 = 0.89) obtained from the literature (Reep, Finlay, and Darlington 2007), a statistically significant difference in slope and intercept was observed between the two groups, such that the slope and intercept for the aquatic Carnivora were found to be significantly lower (p = 0.001).

3.3 | Predictions Based on Regression Analyses on SIM

In addition to the use of PGLS, we also generated a simulated dataset and computed regression statistics (ordinary least squares regression) on these data. A summary of the regression statistics

TABLE 3 | Summary of the regression statistics of the basal nuclei component scaled against brain mass in the Carnivora and Mammals.

Model (*x* variable; *y* variable)	λ	Multiple R^2	Adjusted R^2	Slope	SE	*t* value	*P*	Intercept	SE	*t* value	*P*	Smearing estimator
Carnivora PGLS Brain mass, Caudate mass (EQ 7)	0	0.95	0.94	0.83	0.07	11.92	2.25×10^{-6}	−1.51	0.13	−11.77	2.49×10^{-6}	1.06
Carnivora PGLS brain mass, putamen mass (EQ 8)	0	0.81	0.79	0.98	0.16	5.97	0.0003	−2.66	0.3	−8.76	2.26×10^{-5}	1.07
Carnivora PGLS brain mass, striatum mass (EQ 9)	0	0.94	0.93	0.84	0.07	11.29	3.42×10^{-6}	−1.48	0.14	−10.71	5.06×10^{-6}	1.06
Carnivora PGLS brain mass, globus pallidus mass (EQ 10)	0	0.87	0.85	0.83	0.12	6.83	0.0002	−2.55	0.23	−11.22	9.97×10^{-6}	1.02
Carnivora PGLS brain mass, basal nuclei mass (EQ 11)	0.76	0.99	0.99	0.81	0.02	36.76	2.87×10^{-9}	−1.4	0.05	−26.58	2.73×10^{-8}	1.08
Mammais PGLS brain mass, striatum mass	0.44	0.93	0.93	0.83	0.05	16.97	3.93×10^{-14}	−1.29	0.13	−9.79	1.76×10^{-9}	1.06

Note: All regression statistics were obtained using phylogenetic generalized least squares regression (PGLS). PGLS was performed using Caper (Orme et al. 2018). SE = standard error.

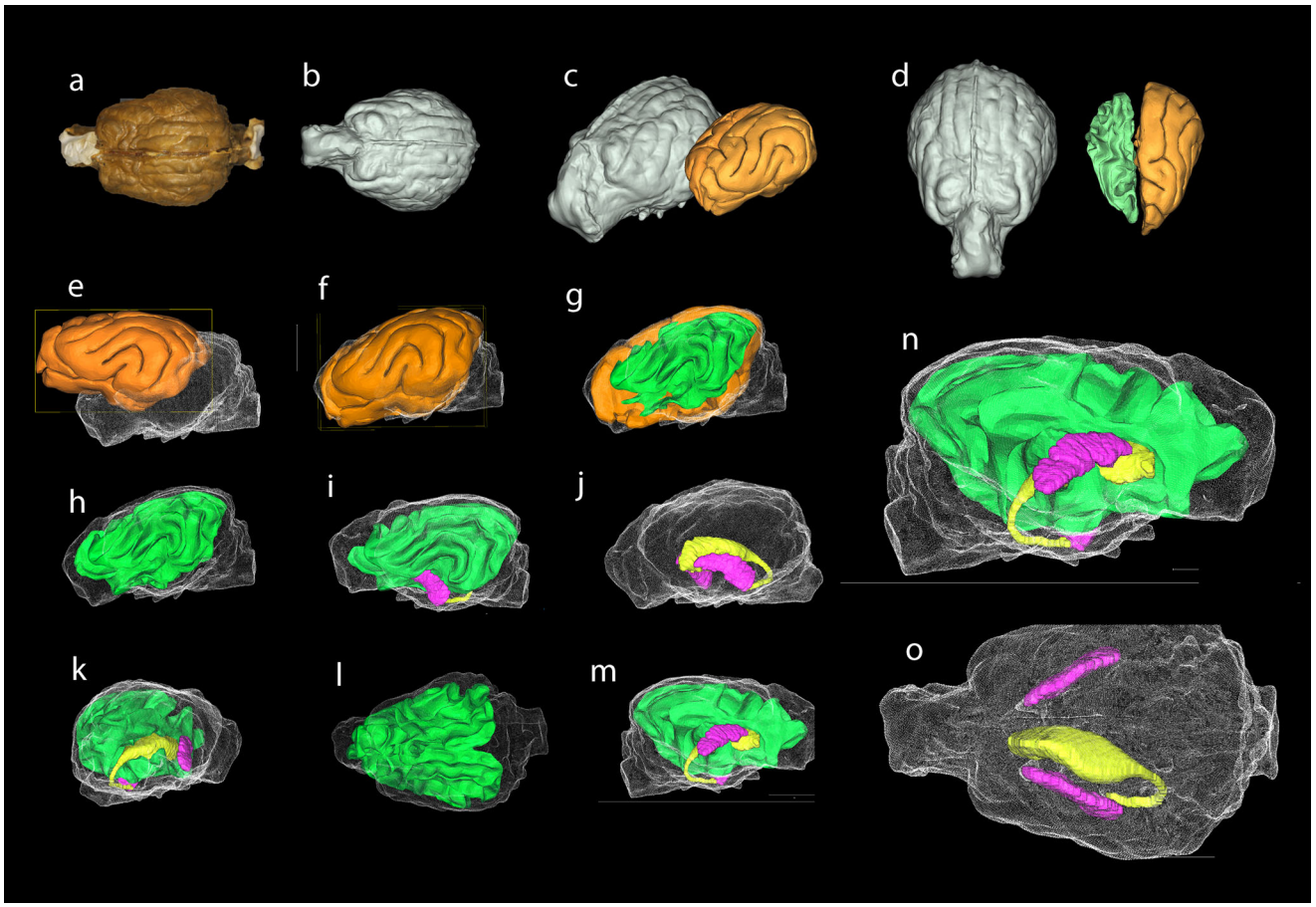

FIGURE 10 | (a–o) Representative images showing different views, alignment and placement of the final white matter, and caudate reconstruction into the 3D point cloud of PM394.

TABLE 4 | Variance: Covariance structure and simulated means for the simulated dataset ($N = 100$).

	SimBrainM	SimCaudM	SimPutM	SimPalliM	SimStriatM	SimBasM
SimBrainM	4795.38	49.076	8.08	4.34	56.79	64.28
SimCaudM	49.08	0.60	0.09	0.05	0.64	0.74
SimPutM	8.08	0.09	0.02	0.01	0.11	0.12
SimPalliM	4.34	0.05	0.01	0.01	0.06	0.06
SimStriatM	56.79	0.64	0.11	0.06	0.80	0.86
SimBasM	64.28	0.74	0.12	0.06	0.86	1.03
Simulated means	SimBrainM = 85.53; SimCaudM = 1.23; SimPutM = 0.19; SimPalliM = 0.12; SimStriatM = 1.47; SimBasM = 1.61					

Note: That the mean values and variance: Covariance structure in this simulated dataset was derived from that observed in the extant Carnivora samples.

and accompanying plots derived from the simulated dataset is shown in Figure 15a–f. All of the simulated variables were characterized by normal distributions with means and variance–covariance structures which coincided with that observed in the extant Carnivora sample (see Table 4). As observed in Figure 15, the simulated caudate and simulated brain mass values were moderately but significantly correlated with one another, with 55% of the variation in caudate mass explained by the variation in brain mass ($P = 6.3 \times 10^{-17}$). The simulated putamen values were weakly ($r^2 = 0.25$) but significantly correlated with simulated brain mass ($P = 8.86 \times 10^{-7}$), as were the simulated pallidal values ($r^2 = 0.25$; $P = 1.12 \times 10^{-10}$), whereas simulated striatal and simulated total basal nuclei mass were moderately but significantly correlated with brain mass ($r^2 = 0.59$; $P = 5.36 \times 10^{-19}$ and $r^2 = 0.54$; $P = 1.81 \times 10^{-16}$, respectively).

Also shown in Figure 16 are the Bland–Altman plots used to assess the limits of agreement between of the congruency in size estimate using the techniques as well as the comparative statistics from the Bland–Altman plots (Table 5). As is apparent from these analyses, there is moderate to strong congruency between the brain component size estimates derived from the two approaches (Figure 16). Bland–Altman plots revealed strong congruency when predicting GI and CT and moderate performance

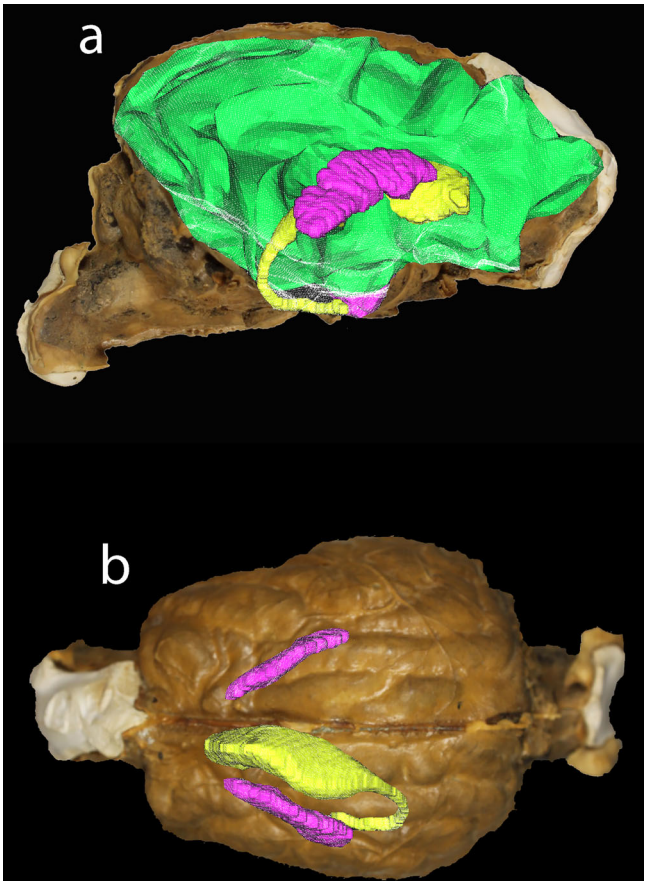

FIGURE 11 | (a–b) Representative images showing 3D views of predicted subcortical reconstructions of the white matter and striatum superimposed on to 2D images of the PM394 (Dire wolf).

when predicting the mass of subcortical structures, with some discrepancy for very small and very large brain masses (Figure 16 and Table 5).

Following the derivation of the above regression statistics, we predicted the size of cortical and subcortical brain components for select fossil Carnivora using both published endocranial volumes as well as the endocranial volumes estimated from digital endocasts. A summary of the regression equation statistics is shown in Table 6. Predictions for the fossil species are tabulated in Table 7.

3.4 | Probabilistic Mapping of Subcortical Anatomy in Fossils

A probabilistic mapping procedure was used to predict and visualize the relative subcortical morphospace for the dire wolf (PM394). Our analyses revealed that the mesh data for the extant Carnivora could be reasonably aligned using manual alignment followed by point to point registration from surface landmarks (Figures 6a–d and 7a–e). As expected, non-transformed mesh overlays were markedly different in size (e.g., Figure 6e,f). However, subsequent transformation (with point to point alignment) resulted in significant overlap between the mesh data and improved the reliability of the resulting probabilistic maps (Figures 8g,h and 9d–g). The overlap in the mesh data was most evident for large areas, including the head and body of the caudate nucleus as well as the mid-rostral to caudal aspects of the white matter maps (Figure 9). For the caudate nucleus, the percentage overlap between the domestic dog and coyote intersecting mesh pair was 38% (476.84 mm^3); for the African wild dog and European wolf, the intersecting volume amounted to 32% (553.27 mm^3); for the tiger and clouded leopard, this was 58% (405.82 mm^3), whereas the cat and fennec fox were 32% (140.45 mm^3). The percentage overlap in intersecting mesh volume for the combined dog, coyote, European wolf, and African wild dog was 15% (431.74 mm^3), whereas the combined intersecting mesh volume for tiger, clouded leopard, cat, and fennec fox was 2% (21.98 mm^3) (Figure 8 and Table 8). For the white matter, the percentage overlap between the domestic dog and coyote intersecting mesh pair was 100% (26,332.16 mm^3); for the combination of dog, coyote, and European wolf, the intersecting volume amounted to 46% (21,016.76 mm^3); for the combination of dog, coyote, European, and maned wolf, this was 30% (17,408.72 mm^3); for the combination of dog, coyote, European wolf, maned wolf, and red fox, this amounted to 18% (13,241.23 mm^3). The percentage overlap for all intersecting white matter mesh volumes was 66% (42,150.48 mm^3).

4 | Discussion

Our results reveal that across the terrestrial Carnivora available to this study, the proportions and scaling of the subcortical nuclei, as well as the size of the overlying cortical GM and GI, were remarkably consistent and strongly predictable from brain mass.

4.1 | Interpretational Considerations: Mechanisms of Change and Model Assumptions

When interpreting the results of our predictions of brain component size for the fossil taxa and their moderate to high predictability from brain size, it is important to keep in mind that these scaling analyses do not negate the influence of adaptive or mosaic changes in brain evolution (Barton 2001; Barton and Harvey 2000). That adaptive change exists and helps to describe species differences in brain structure and function is undeniable. These results may be interpreted as indicating that relative brain structure size is rather invariant across species. This would suggest that investigators seeking to identify specializations in the function of the brain components included in this study are likely to uncover these adaptive changes at cellular, receptor, and/or genetic levels of organization not covered in our analyses. It is, however, important to note that the proportion of striatal integration with other regions (and the required relative mass) might still vary widely in species not covered in our analyses (i.e., aquatic Carnivora) as has been argued for primates (Yin et al. 2009).

Furthermore, it is important to acknowledge the assumptions which underlie that this work as predictions can only be made given a set of assumptions. When predicting fossil patterns based on an extant data, the predictive assumptions are the same assumptions as those made when inferring patterns of evolution based solely on extant variation. For example, in the current study, we used the underlying variance:covariance and correlational

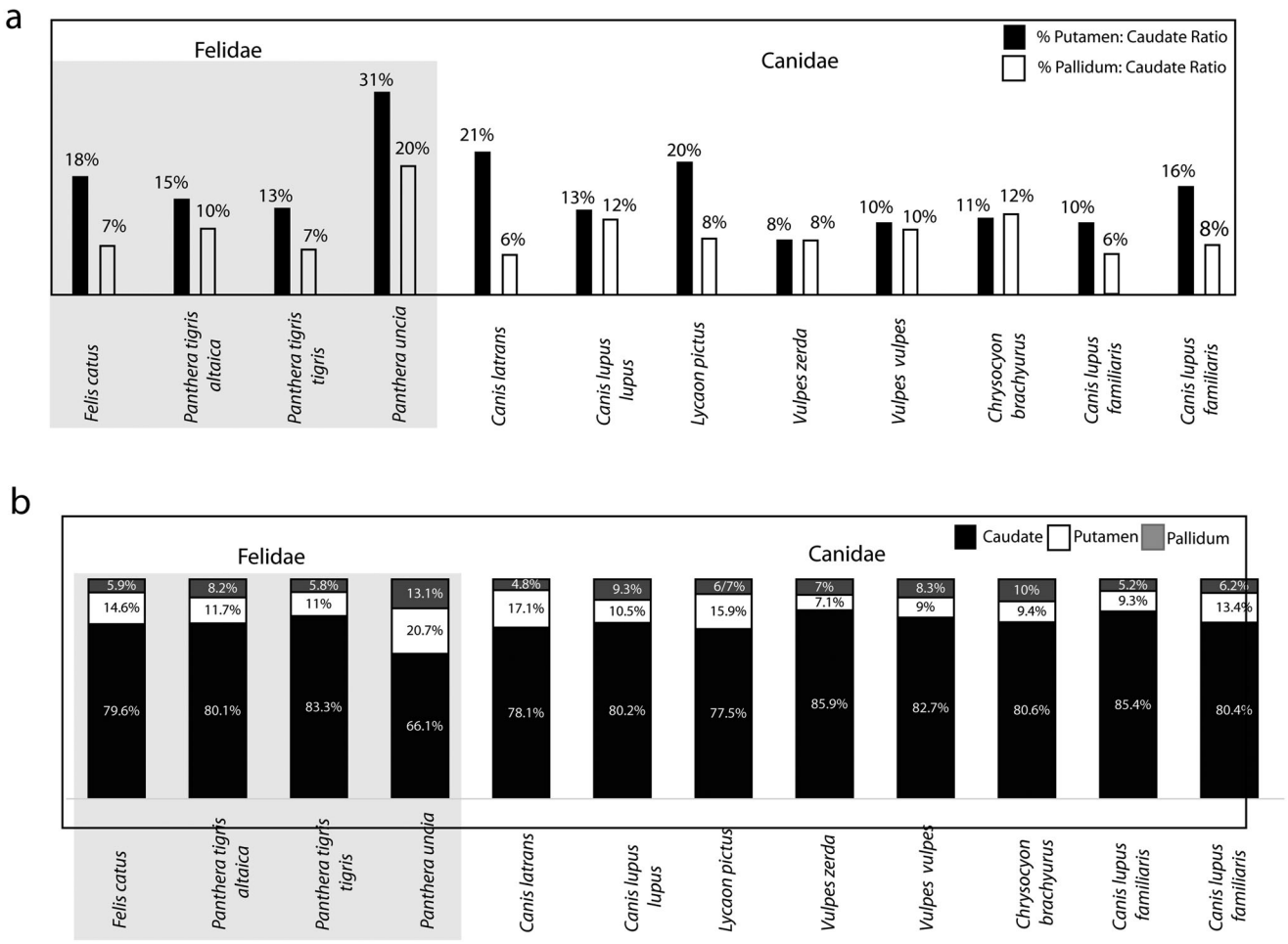

FIGURE 12 | (a) Box plots showing the percentage putamen mass to caudate mass ratio and percentage pallidal mass to caudate mass ratio in select Carnivora species. (b) Box plots showing the proportional contribution to total mass (i.e., caudate + nucleus accumbens + putamen + external globus pallidus) that the caudate, putamen and external globus pallidus contribute in each species.

structure observed in extant species as a starting point for our simulation analyses. The assumption in this case is that the range of variation observed in extant species is consistent with that expected for fossil species. This principle of uniformitarianism is a fundamental operational principle in paleobiology, allowing for the transposition of present causes as explanatory factors for the distant past (Scott 1963) and is a necessary assumption to facilitate predictions of brain component size in fossil taxa. An unintentional consequence of this assumption is that it creates an entanglement of the fossil and extant data, reducing the independent explanatory power of the fossils to mere placeholders that align with our understanding derived from extant species. In the absence of any direct fossilized subcortical brain data, this complex entanglement is an unavoidable contingency for which the authors have no solution at present.

Similarly, assumptions on how evolution may have unfolded are also entangled with the derived fossil predictive equations. For instance, in the current study, the use of PGLS assumes a Brownian motion model, where variation has accumulated proportional to time along each lineage with no significant phenotypic variation along any individual lineage, and the rate of evolution is stochastically constant across all branches (Smears, Mongle, and Kandler 2016). This assumption is an inevitable and necessary construct of phylogenetic regression, one that does not invalidate its use over traditional regression approaches but is worth remembering as another example of this complex entanglement of fossil and extant data. Furthermore, this entanglement is also reified through the assumption that the range of variation observed in extant species is consistent with that expected for fossil species. This is a hallmark of the standard Brownian motion model of evolution, where the model assumption is that predictions are only meaningful if the data evolves following a Brownian model of evolution such that fossil variation is consistent with extant variation.

4.2 | Putamen:Caudate, Pallidal:Caudate, and Pallidal:Putamen Ratios

In our analysis of basal nuclei proportionality (Figure 12), we generally observed consistency across the taxa. Most notably, in most canids, the proportion of the caudate nucleus to total basal nuclei mass ranged between 78% and 86%, putamen between 7% and 17%, and external globus pallidus between 5% and 10% of total basal nuclei mass. Amongst the canids, the red and fennec fox had the smallest proportion of total basal nuclei mass composed of the putamen and external globus pallidus (putamen 7%–9%; external

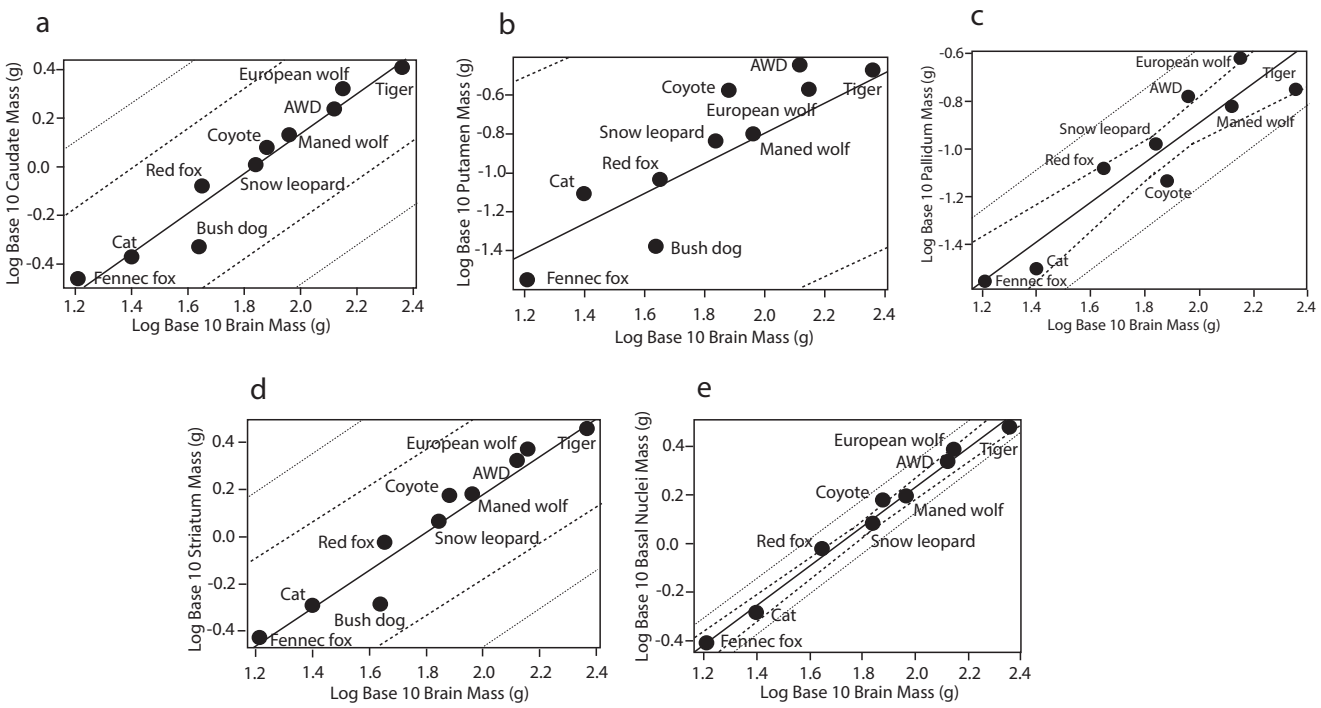

FIGURE 13 | Plots derived from phylogenetic generalized least squares regression (PGLS) analysis of the extant data. (a) brain mass plotted against whole caudate mass; (b) brain mass plotted against putamen mass, (c), brain mass plotted against pallidal mass; (d) brain mass plotted against striatal mass; (e) brain mass plotted against basal nuclei mass. All data were logarithmically transformed (base 10) prior to inclusion in the regression analyses. Data used to derive these relationships are shown in Table 1. Dotted lines indicate the prediction and confidence intervals for each regression line.

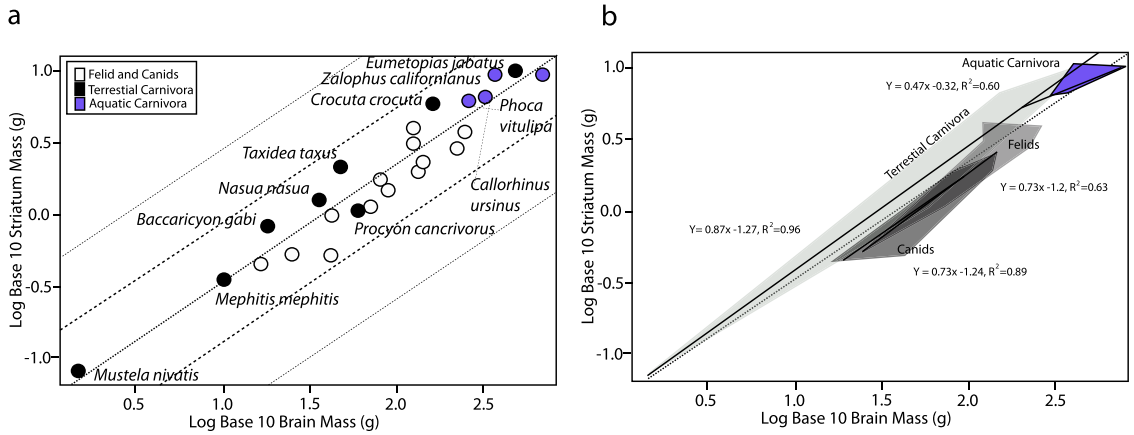

FIGURE 14 | Bivariate PGLS regression analysis plots (a) and accompanying convex hulls (b) derived from brain mass and striatal mass data for the aquatic and terrestrial Carnivora. Data used in these analyses were collated from the literature (See Reep, Finaly, and Darlington 2007) and combined with species data points from the current study. Dotted lines indicate the prediction and confidence intervals for each regression line. Note the marked difference in slope and regression statistics between terrestrial and aquatic Carnivora.

globus pallidus 7%–8%). This observation was quite distinct from that observed in the wolf-like canids where the putamen proportionality made up a larger percentage of total basal nuclei mass (9.4%–17%), suggestive of a phylogenetic and functional difference between fox-like and wolf-like canids. Similarly, for the felids, we observed a marked difference in the proportionality of the caudate nucleus in the snow leopard relative to the other felids. All other felids displayed caudate proportionality ranging between 79% and 83% of total basal nuclei size, whereas the snow leopard caudate only made up a total of 66% of total basal nuclei size. The reduction in snow leopard caudate proportionality was accompanied by a proportional increase in both the putamen and external globus pallidus for this species, which was markedly larger (proportionally) from that observed in the other cats. We propose that the above examples of species level variation in basal nuclei proportionality may provide a basis for potential species level differences in behavior.

It is important to note, however, that our observation of high predictability using this species-level comparison does not negate

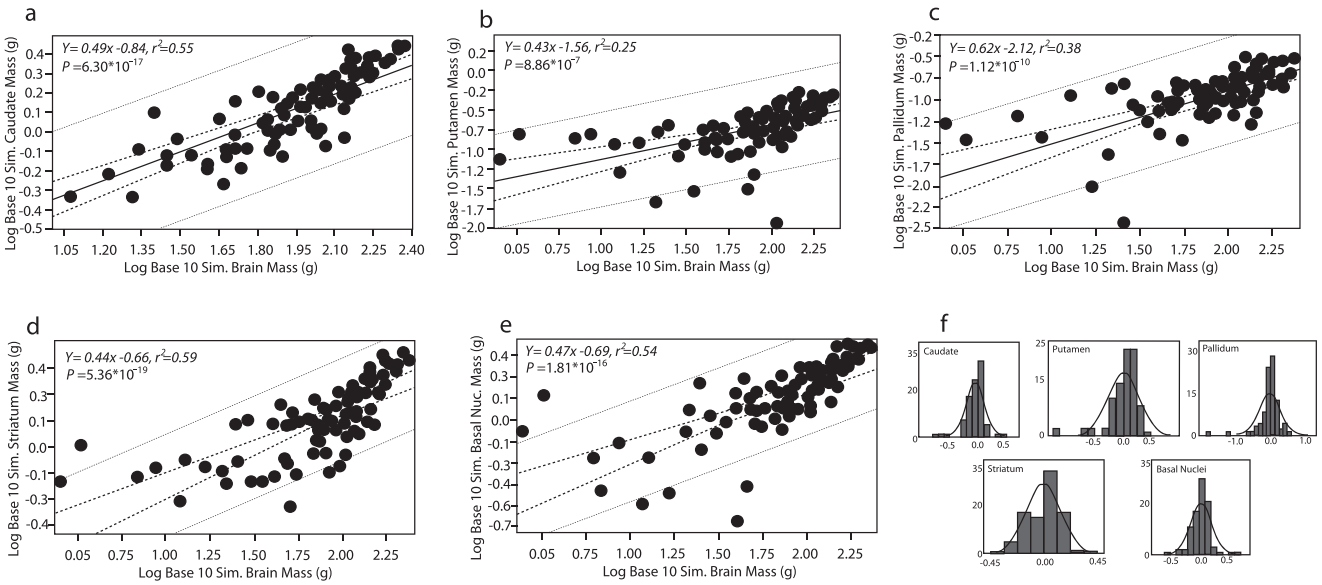

FIGURE 15 | Plots derived from ordinary least squares regression (OLS) of the simulation data (SIM). The simulated dataset of $N = 100$ individuals, was generated using the variance–covariance structure observed in our extant sample. Least squares regression analysis was applied to the log transformed simulated dataset and a new set of predictive equations were calculated. (a) Simulated brain mass plotted against Simulated caudate mass; (b) Simulated brain mass plotted against Simulated putamen mass, (c) Simulated brain mass plotted against Simulated pallidal mass; (d) Simulated brain mass plotted against Simulated striatal mass; (e) Simulated brain mass plotted against Simulated basal nuclei mass. All data were logarithmically transformed (base 10) prior to inclusion in the regression analyses. Dotted lines indicate the prediction and confidence intervals for each regression line. (f) normal probability plots of the simulated data. Note the marked difference in slope and regression statistics between the PGLS and Simulated regressions. Despite these difference in slope, the bivariate relationships were still significant ($p < 0.05$) and explained between 25% and 55% of the variation in Y variable.

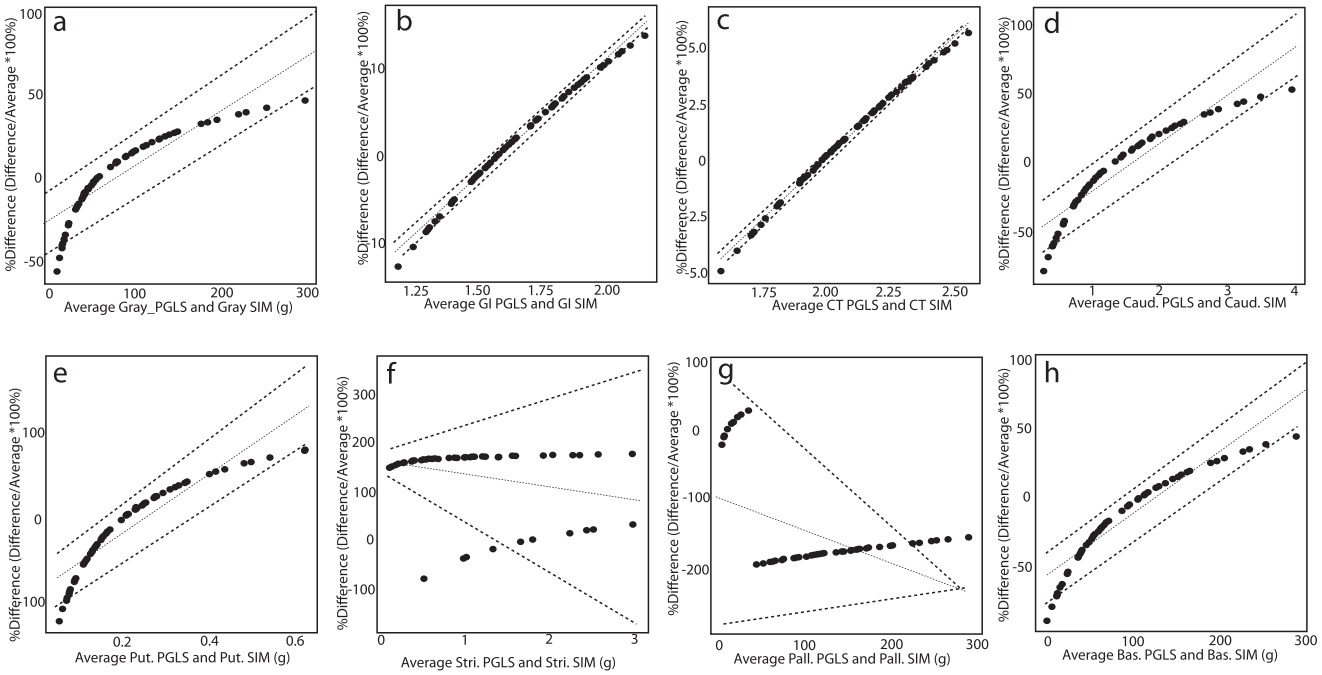

FIGURE 16 | (a–h) Bland–Altman plots showing the limits of agreement between estimate values derived from the extant PGLS sample and Simulation sample. CT, cortical thickness; PGLS, phylogenetic generalized least squares regression; SIM, simulation data.

TABLE 5 | Bland & Altman Statistics derived in BA-plotteR (Goedhart and Rishniw 2021) for assessing the limits of agreement between fossil brain component estimates derived from the phylogenetic generalized least squares (PGLS) and simulation equations used in the current study.

Bland & Altman plot statistics	Parameter	Value	95% CI lower limit	95% CI upper limit
Gray PGLS versus Gray SIM	Difference	−0.15	−5.82	5.52
	Intercept	−25.56	−29.48	−21.63
	Slope	0.33	0.29	0.37
GI PGLS versus GI SIM	Difference	1.88	0.42	3.33
	Intercept	−43.54	−44.52	−42.55
	Slope	27.12	26.54	27.7
CT PGLS versus CT SIM	Difference	0.85	0.27	1.43
	Intercept	−22.59	−22.96	−22.22
	Slope	11.37	11.19	11.55
Caudate PGLS versus Caudate SIM	Difference	−7.54	−14.88	−0.21
	Intercept	−54.54	−59.52	−49.56
	Slope	34.42	31.29	37.56
Putamen PGLS versus Putamen SIM	Difference	−15.11	−26.56	−3.65
	Intercept	−82.1	−90.07	−74.14
	Slope	335.14	301.59	368.68
Striatum PGLS versus Striatum SIM	Difference	141.73	126.1	157.36
	Intercept	166.26	141.58	190.94
	Slope	−25.03	−45.08	−4.98
Pallidum PGLS versus Pallidum SIM	Difference	−147.24	−162.69	−131.79
	Intercept	−93.97	−121.72	−66.21
	Slope	−73.76	−107.28	−40.25
Basal Nuclei PGLS versus Basal Nuclei SIM	Difference	−17.79	−25	−10.59
	Intercept	−66.32	−71.08	−61.56
	Slope	28.81	26.36	31.27

Abbreviations: CT, cortical thickness; GI, gyrification index; PGLS, phylogenetic generalized least squares regression; SIM, simulation data.

the existence of meaningful interspecific or individual variation in these parameters. A prime example of this is that observed for the two domestic dogs included in this study where the proportion of the putamen:caudate and pallidal:caudate varied between 10%–16% and 6%–8%, respectively.

4.3 | Predictions Based on Regression Analyses of Extant and SIM

Despite our observations of individual and species differences in basal nuclei proportionality, regression analyses revealed that there is large consistency in the scaling of subcortical brain components in Carnivora and that this can be used to accurately predict brain component size accurately from whole brain size. Our analyses using both a simulated data set and that provided directly from extant Carnivora aligned well with this conclusion. As with previous investigators, we interpret this consistency in scaling attributes as reflective of the underlying constraints (i.e., architectural, developmental, energetic, or phylogenetic) that govern structural laws of form (Manger, Spocter & Patzke 2013). To this end, we predicted the size of cortical and subcortical brain components for the fossil Carnivora with these analyses, revealing significant congruency in size estimates using the two different data sources (Table 8). A comparison of the limits of agreement using Bland–Altman plots (as well as accompanying statistics) revealed strong congruency between estimates when predicting GI and CT using the two approaches, whereas other estimates performed moderately (GM, caudate, putamen, and total basal nuclei mass), with some divergence for very small and very large brain masses (Figure 16 and Table 6). These results potentially highlight the usefulness of simulated data to supplement an extant dataset and aid in allometric prediction when samples size is limited.

Although our regression statistics were largely consistent between terrestrial Carnivora (including felids and canids), this was not the case for the aquatic Carnivora where the slope of striatal mass: Brain mass scaling was markedly lower (Figure 14). Although our sample size is rather small in this current dataset, it is possible that this observation points to a relaxation of the constraints that couple brain to brain component size in aquatic Carnivora and permitting a relative increase in brain size for these species. Some evidence that such scaling differences do

TABLE 6 | Regression equation formulae, coefficients of determination (R^2) and associated log transformation bias (Smearing estimator) derived in the current study.

Equation formulae	Method	R^2	Smearing estimator
EQ 1: Log 10 gray mass (g) = 1.0274 × Log 10 brain mass (g) − 0.17196	PGLS-Extant	0.99	1.00
EQ 2: Log 10 GI = 0.17831 × Log 10 brain mass (g) − 0.10912	PGLS-Extant	0.94	1.00
EQ 3: Log 10 CT = 0.12527 × Log 10 brain mass (g) + 0.079529	PGLS-Extant	0.73	1.00
EQ 4: Log 10 gray mass (g) = 0.76734 × Log 10 brain mass (g) + 0.31487	Simulation -OLS	0.46	1.30
EQ 5: Log 10 GI = 0.11227 × Log 10 brain mass (g) + 0.0061692	Simulation -OLS	0.36	1.02
EQ 6: Log 10 CT = 0.099041 × Log 10 brain mass (g) + 0.12487	Simulation -OLS	0.31	1.02
EQ 12: Log 10 caudate mass (g) = 0.49017 × Log 10 brain mass (g) − 0.84111	Simulation -OLS	0.55	1.11
EQ 13: Log 10 putamen mass (g) = 0.43006 × Log 10 brain mass (g) − 1.562	Simulation -OLS	0.25	1.41
EQ 14: Log 10 pallidal mass (g) = 0.61536 × Log 10 brain mass (g) − 2.1249	Simulation -OLS	0.62	1.12
EQ 15: Log 10 striatal mass (g) = 0.43809 × Log 10 brain mass (g) − 0.66175	Simulation -OLS	0.59	1.06
EQ 16: Log 10 basal nuclei mass (g) = 0.47406 × Log 10 brain mass (g) − 0.69273	Simulation -OLS	0.54	1.09

Abbreviations: CT, cortical thickness; GI, gyrification index; OLS, ordinary least squares; PGLS, phylogenetic generalized least squares regression.

exist in the Carnivora is most evident for the olfactory system, where aquatic Carnivora are known to have a markedly reduced olfactory system and bulbs (Welker et al. 2006) a pattern that is also observed in the aquatic Afrotheria (Reep et al. 1989). There are also notable differences in gyrencephaly between seals and other terrestrial carnivores (Lyras et al. 2016; Manger et al. 2012). These differences between aquatic and terrestrial Carnivora are intriguing and warrant further analysis in explaining cognitive, behavioral, and ecological differences between these groups.

Our results demonstrated a robust relationship between brain volume and gyrification in the extant species. In contrast, Lyras et al. (2016) observed an increase in both external cortical area and gyrification in the Carnivora, which was unrelated to brain size. These observations might contribute additional variation in cortical area estimates, particularly for deep-time taxa not captured by our current set of analyses.

4.4 | Probabilistic Mapping of Subcortical Anatomy in Fossils

Probabilistic mapping of subcortical structures in the fossil carnivore revealed that the approach has some merit for predicting and visualizing the subcortical morphospace. We found large areas of overlap in the transformed mesh data of the extant Carnivora included in our analyses. Notably, the percentage overlap was greatest in more closely related species as was seen for comparisons that only included "wolf-like" canids, whereas the percentage overlap was influenced by the inclusion of "fox-like" canids and felids. Although our approach is exploratory, we envisage that further development and integration of these techniques with other data sources could greatly aid comparative analyses by allowing researchers to make more accurate inferences about fossil species behavior and cognitive capabilities. Furthermore, probabilistic-based predictions of the shape and size of brain structure in fossil species may also dramatically assist in the fossil reconstruction process. Due to the variability of taphonomic processes, it is likely that a paleoneurologist might only have a partial or incomplete surface of the endocast (or cranium) from which to work. In such cases, these approaches (applied to both predictions of the internal and external endocast structure) would help increase sample size by including predictive data from fragmentary remains.

5 | Conclusion

We propose that the current set of analyses demonstrate the utility of predicting and visualizing species brain component size in fossil taxa. The use of brain size to derive further insight into the neurobiology of fossil species is notable as this single variable is often the only available data from which to directly assess brain evolution in the fossil record. Furthermore, here we demonstrate how modern 3D imaging techniques can be leveraged to make probabilistic predictions of subcortical brain anatomy in fossils. We hope that this study and accompanying data will serve as an additional resource and promote dialogue between neurobiologists working on extant Carnivora models as well as paleoneurologists describing the nervous systems of

TABLE 7 | Estimated species average cortical gray matter (GM), gyrification index (GI), cortical thickness (CT), caudate mass (CM), putamen mass (PM), striate mass (SM), pallidal mass (PalM) and basal nuclei mass (BasM) for the fossil Carnivora.

Specimen # or Species	Refs	BM (g)	Eq. 1 GM	Eq. 2 GI	Eq. 3 CT	Eq. 4 GM	Eq. 5 GI	Eq. 6 CT	Eq. 7 CM	Eq. 8 PM	Eq. 9 SM	Eq. 10 PalM	Eq. 11 BasM	Eq. 12 CM	Eq. 13 PM	Eq. 14 PalM	Eq. 15 SM	Eq. 16 BasM
PM58861 *Dinobastis*	Current	261.831	205.265	2.099	2.412	148.018	1.895	2.314	3.140	0.512	3.557	0.286	3.619	2.209	0.301	0.231	2.498	2.842
PM58862 *Metailurus*	Current	106.416	81.393	1.788	2.155	74.178	1.713	2.117	1.487	0.212	1.670	0.136	1.745	1.421	0.204	0.133	1.684	1.854
PM58868 *Ischyrosmilus*	Current	201.817	157.092	2.004	2.335	121.215	1.841	2.255	2.530	0.397	2.859	0.231	2.931	1.944	0.269	0.197	2.229	2.512
PM58870 *Pseudaelurus*	Current	74.752	56.624	1.679	2.062	56.568	1.646	2.044	1.109	0.150	1.241	0.101	1.311	1.195	0.175	0.107	1.442	1.568
PM58872 *Proailurus*	Current	45.690	34.146	1.538	1.938	38.772	1.558	1.947	0.737	0.093	0.821	0.067	0.880	0.939	0.142	0.079	1.163	1.242
PM58951 *Aelurodon*	Current	121.165	93.004	1.830	2.190	81.946	1.738	2.144	1.657	0.241	1.862	0.151	1.939	1.514	0.216	0.144	1.782	1.972
PM58953 *Canis lepophagus*	Current	47.881	35.829	1.550	1.950	40.191	1.566	1.956	0.767	0.097	0.854	0.070	0.914	0.960	0.145	0.081	1.187	1.270
PM394 *Canis dirus*	Current	169.653	131.429	1.943	2.285	106.096	1.805	2.217	2.190	0.335	2.471	0.200	2.547	1.785	0.249	0.177	2.065	2.313
PM58963 *Borophagus*	Current	194.141	150.956	1.990	2.324	117.661	1.833	2.246	2.450	0.382	2.767	0.223	2.840	1.907	0.264	0.192	2.191	2.466
PM58961 *Leptocyon Sp.*	Current	15.018	10.886	1.261	1.686	16.509	1.375	1.743	0.293	0.031	0.322	0.027	0.357	0.544	0.088	0.040	0.714	0.733
Aelurodon taxoides	1*	154.001	118.988	1.910	2.257	98.502	1.786	2.195	2.021	0.305	2.278	0.184	2.354	1.703	0.239	1.980	0.166	2.209
Aelurodon ferox	1*	139.238	107.285	1.876	2.229	91.172	1.765	2.174	1.859	0.276	2.093	0.170	2.170	1.621	0.229	1.894	0.156	2.106
Aelurodon asthenostylus	1*	95.633	72.932	1.754	2.126	68.339	1.693	2.094	1.361	0.191	1.527	0.124	1.601	1.348	0.195	1.607	0.124	1.763
Aelurodon mcgrewi	1*	64.843	48.927	1.637	2.025	50.721	1.620	2.015	0.986	0.131	1.101	0.090	1.168	1.114	0.165	1.355	0.098	1.466
Borophagus littoralis	1*	131.593	101.237	1.857	2.213	87.305	1.754	2.162	1.774	0.261	1.996	0.162	2.073	1.576	0.224	1.848	0.151	2.051
Borophagus secundus	1*	123.460	94.814	1.836	2.196	83.135	1.742	2.148	1.683	0.245	1.892	0.153	1.969	1.528	0.218	1.797	0.145	1.990

(Continues)

TABLE 7 | (Continued)

Specimen # or Species	Refs	BM (g)	Eq. 1 GM	Eq. 2 GI	Eq. 3 CT	Eq. 4 GM	Eq. 5 GI	Eq. 6 CT	Eq. 7 CM	Eq. 8 PM	Eq. 9 SM	Eq. 10 PalM	Eq. 11 BasM	Eq. 12 CM	Eq. 13 PM	Eq. 14 PalM	Eq. 15 SM	Eq. 16 BasM
Carpocyon webbi	1*	104.429	79.832	1.782	2.150	73.112	1.709	2.113	1.464	0.208	1.644	0.134	1.719	1.408	0.202	1.670	0.131	1.838
Carpocyon compressus	1*	74.198	56.193	1.676	2.060	56.247	1.645	2.042	1.103	0.149	1.233	0.101	1.303	1.190	0.175	1.438	0.106	1.563
Cormocyon copei	1*	25.796	18.979	1.389	1.804	25.004	1.461	1.839	0.459	0.053	0.508	0.042	0.554	0.709	0.111	0.905	0.055	0.947
Desmocyon mathewi	1*	40.010	29.793	1.502	1.906	35.017	1.535	1.921	0.660	0.081	0.734	0.060	0.790	0.879	0.134	1.097	0.073	1.166
Desmocyon thompsoni	1*	38.083	28.320	1.488	1.895	33.716	1.526	1.912	0.634	0.077	0.704	0.058	0.759	0.858	0.131	1.073	0.070	1.139
Epicyon haydeni	1*	135.996	104.719	1.868	2.222	89.538	1.761	2.169	1.823	0.270	2.052	0.166	2.129	1.602	0.227	1.875	0.154	2.083
Epicyon saevus	1*	107.858	82.526	1.792	2.159	74.948	1.716	2.119	1.504	0.215	1.689	0.137	1.764	1.430	0.205	1.694	0.134	1.866
Microtomarctus conferta	1*	36.187	26.872	1.475	1.883	32.420	1.518	1.902	0.608	0.074	0.675	0.055	0.729	0.837	0.128	1.050	0.068	1.112
Otarocyon cooki	1*	11.437	8.229	1.201	1.630	13.396	1.333	1.697	0.234	0.024	0.256	0.021	0.287	0.476	0.078	0.634	0.034	0.644
Otarocyon macdonaldi	1*	8.153	5.812	1.131	1.562	10.332	1.284	1.641	0.176	0.017	0.193	0.016	0.218	0.403	0.068	0.546	0.027	0.549
Paracynarctus sinclairi	1*	61.735	46.519	1.622	2.013	48.845	1.611	2.005	0.947	0.124	1.057	0.086	1.123	1.088	0.161	1.326	0.095	1.432
Paracynarctus euthos	1*	62.098	46.800	1.624	2.014	49.065	1.612	2.007	0.951	0.125	1.062	0.087	1.128	1.091	0.162	1.330	0.095	1.436
Paracynarctus temerarius	1*	55.934	42.034	1.594	1.988	45.282	1.594	1.986	0.872	0.113	0.973	0.080	1.037	1.036	0.155	1.270	0.089	1.367
Phlaocyon multicuspus	1*	24.719	18.165	1.378	1.795	24.199	1.454	1.832	0.443	0.051	0.490	0.040	0.535	0.695	0.109	0.888	0.054	0.928
Phlaocyon leocosteus	1*	19.653	14.352	1.323	1.744	20.294	1.417	1.790	0.366	0.041	0.404	0.033	0.444	0.621	0.099	0.803	0.047	0.833
Protomarctus optatus	1*	56.752	42.666	1.598	1.992	45.790	1.596	1.989	0.883	0.115	0.985	0.081	1.049	1.044	0.156	1.278	0.090	1.376
Rhizocyon oregonensis	1*	17.892	13.032	1.301	1.724	18.883	1.402	1.774	0.339	0.037	0.373	0.031	0.412	0.593	0.095	0.771	0.044	0.796

(Continues)

TABLE 7 | (Continued)

Specimen # or Species	Refs	BM (g)	Eq. 1 GM	Eq. 2 GI	Eq. 3 CT	Eq. 4 GM	Eq. 5 GI	Eq. 6 CT	Eq. 7 CM	Eq. 8 PM	Eq. 9 SM	Eq. 10 PalM	Eq. 11 BasM	Eq. 12 CM	Eq. 13 PM	Eq. 14 PalM	Eq. 15 SM	Eq. 16 BasM
Tomarctus hippophaga	1*	70.500	53.317	1.661	2.047	54.083	1.636	2.032	1.057	0.142	1.182	0.096	1.250	1.161	0.171	1.406	0.103	1.526
Tomarctus brevirostris	1*	53.147	39.884	1.580	1.976	43.541	1.584	1.976	0.836	0.107	0.932	0.076	0.995	1.011	0.151	1.242	0.086	1.334
Alopex lagopus	1*	36.799	27.339	1.479	1.887	32.839	1.520	1.905	0.616	0.075	0.684	0.056	0.738	0.844	0.129	1.057	0.069	1.121
Atelocynus microtis	1*	64.418	48.598	1.635	2.024	50.466	1.619	2.014	0.981	0.130	1.095	0.089	1.162	1.111	0.164	1.351	0.097	1.462
Canis dirus	1*	184.056	142.906	1.971	2.308	112.942	1.822	2.235	2.344	0.363	2.646	0.214	2.720	1.858	0.258	2.140	0.186	2.404
Canis armbrusteri	1*	158.953	122.921	1.920	2.266	100.924	1.792	2.202	2.075	0.314	2.339	0.189	2.416	1.729	0.242	2.007	0.170	2.243
Cuon javanicus	1*	121.409	93.196	1.830	2.191	82.073	1.738	2.144	1.659	0.241	1.865	0.151	1.942	1.515	0.216	1.784	0.144	1.974
Euocyon davisi	1*	57.684	43.386	1.603	1.996	46.366	1.599	1.992	0.895	0.116	0.998	0.082	1.063	1.052	0.157	1.288	0.091	1.387
Leptocyon vafer	1*	25.082	18.439	1.382	1.798	24.471	1.456	1.834	0.448	0.051	0.496	0.041	0.541	0.700	0.110	0.894	0.054	0.935
Leptocyon gregorii	1*	15.820	11.484	1.273	1.697	17.182	1.383	1.752	0.306	0.033	0.337	0.028	0.373	0.558	0.090	0.730	0.041	0.751
Nyctereutes cf.donnezani	1*	55.374	41.602	1.591	1.986	44.934	1.592	1.984	0.865	0.112	0.965	0.079	1.028	1.031	0.154	1.265	0.089	1.361
Nyctereutes donnezani	1*	55.374	41.602	1.591	1.986	44.934	1.592	1.984	0.865	0.112	0.965	0.079	1.028	1.031	0.154	1.265	0.089	1.361
Cynodesmus thooides	1*	39.130	29.119	1.496	1.901	34.424	1.531	1.917	0.648	0.080	0.721	0.059	0.776	0.870	0.133	1.086	0.072	1.154
Enhydrocyon basilatus	1*	76.332	57.854	1.685	2.067	57.484	1.650	2.048	1.129	0.153	1.263	0.103	1.334	1.207	0.177	1.456	0.108	1.584
Enhydrocyon stenocephalus	1*	71.598	54.171	1.666	2.051	54.728	1.638	2.035	1.070	0.144	1.197	0.098	1.266	1.170	0.172	1.415	0.104	1.537
Enhydrocyon pahinsinte-wakpa	1*	56.068	42.138	1.595	1.989	45.366	1.594	1.986	0.874	0.113	0.975	0.080	1.039	1.038	0.155	1.272	0.089	1.369
Hesperocyon gregarius	1*	15.416	11.183	1.267	1.692	16.844	1.379	1.748	0.299	0.032	0.330	0.027	0.365	0.551	0.089	0.722	0.040	0.742
Mesocyon coryphaeus	1*	49.904	37.386	1.562	1.960	41.488	1.573	1.964	0.793	0.101	0.884	0.072	0.945	0.980	0.147	1.208	0.083	1.295

(Continues)

TABLE 7 | (Continued)

Specimen # or Species	Refs	BM (g)	Eq. 1 GM	Eq. 2 GI	Eq. 3 CT	Eq. 4 GM	Eq. 5 GI	Eq. 6 CT	Eq. 7 CM	Eq. 8 PM	Eq. 9 SM	Eq. 10 PalM	Eq. 11 BasM	Eq. 12 CM	Eq. 13 PM	Eq. 14 PalM	Eq. 15 SM	Eq. 16 BasM
Mesocyon brachyops	1*	40.767	30.372	1.507	1.911	35.524	1.538	1.925	0.671	0.083	0.746	0.061	0.802	0.888	0.135	1.106	0.073	1.177
Osbornodon fricki	1*	104.864	80.174	1.783	2.151	73.346	1.710	2.113	1.469	0.209	1.649	0.134	1.725	1.410	0.203	1.673	0.131	1.841
Osbornodon Iamonensis	1*	65.641	49.546	1.640	2.028	51.199	1.622	2.018	0.996	0.132	1.113	0.091	1.180	1.121	0.166	1.362	0.098	1.475
Paraenhydodon josephi	1*	41.481	30.919	1.511	1.915	36.001	1.541	1.928	0.680	0.084	0.757	0.062	0.814	0.895	0.136	1.114	0.074	1.186
Sunkahetanka geringensis	1*	56.659	42.594	1.598	1.991	45.732	1.596	1.988	0.881	0.114	0.983	0.080	1.047	1.043	0.156	1.277	0.090	1.375
Homotherium hadarensis	1*	211.510	164.848	2.021	2.349	125.658	1.850	2.266	2.630	0.416	2.974	0.240	3.045	1.989	0.274	2.275	0.202	2.568
Homotherium serus	1*	332.290	262.209	2.190	2.485	177.718	1.947	2.369	3.827	0.647	4.346	0.349	4.390	2.482	0.333	2.773	0.267	3.181
Lynx shansius	1*	68.320	51.624	1.652	2.039	52.795	1.630	2.026	1.030	0.137	1.151	0.094	1.219	1.143	0.169	1.387	0.101	1.503
Machairodus palenderi	1*	291.040	228.826	2.139	2.444	160.531	1.918	2.338	3.428	0.568	3.888	0.313	3.943	2.326	0.315	2.616	0.246	2.988
Nimravides galiani	1*	217.290	169.479	2.030	2.357	128.284	1.856	2.272	2.690	0.427	3.042	0.245	3.112	2.016	0.277	2.302	0.206	2.601
Panthera atrox	1*	459.870	366.127	2.321	2.589	228.043	2.019	2.447	5.012	0.890	5.710	0.457	5.711	2.911	0.383	3.197	0.326	3.711
Panthera Augusta	1*	272.660	213.992	2.114	2.425	152.693	1.904	2.323	3.248	0.533	3.681	0.296	3.740	2.253	0.306	2.543	0.237	2.897
Pseudaelurus validus	1*	71.790	54.320	1.667	2.051	54.841	1.639	2.036	1.073	0.144	1.200	0.098	1.269	1.171	0.172	1.417	0.104	1.539
Smilodon californicus	1*	385.610	305.526	2.249	2.532	199.216	1.979	2.404	4.330	0.749	4.925	0.395	4.952	2.670	0.355	2.959	0.293	3.414
Smilodon fatalis	1*	345.910	273.257	2.206	2.498	183.281	1.955	2.379	3.957	0.673	4.495	0.361	4.535	2.532	0.339	2.822	0.274	3.243
Smilodon gracilis	1*	184.880	143.563	1.973	2.309	113.330	1.823	2.236	2.352	0.364	2.656	0.215	2.730	1.862	0.259	2.145	0.186	2.409

Note: Equations 1–3 and 7–11 were derived using the regression statistics for $N = 6$ extant Canidae (See Grewal et al. 2020). The remaining equations that is, 4–6 and 12–16 were derived through simulation ($N = 100$) using the variance–covariance relationship observed in the extant Carnivora. Note that the masses provided in the table have not been multiplied by the Smearing estimator for each equation. When using any masses from this table please, multiply the mass by the associated Smearing estimator calculated in Table 6. 1* = Finarelli and Flynn (2009). "Brain-Size Evolution and Sociality in Carnivora." *PNAS* 106, no. 23: 9345–9349.

TABLE 8 | Intersecting volumes (mm^3) and associated percentage overlap calculated for intersecting mesh combinations of the caudate nucleus and white matter.

Overlapping mesh (caudate Intersections)	Intersection volume	% overlap of components	% overlap of total
Dog-Coyote	476.85	38.16	11.62
African wild dog-European wolf	553.27	32.07	13.49
Tiger-Clouded Leopard	405.82	58.68	9.89
Cat-Fennec fox	140.46	32.25	3.42
Dog-Coyote-African wild dog-European wolf	431.74	14.51	10.52
Tiger-Clouded Leopard-Cat-Fennec fox	21.98	1.95	0.54
Overlapping mesh (white matter Intersections)	**Intersection volume**	**% overlap of components**	**% overlap of total**
Dog-Coyote	26,332.16	100	28.71
Dog-Coyote-European wolf	21,016.76	46.14	22.91
Dog-Coyote-European wolf-Maned wolf	17,408.72	29.67	18.98
Dog-Coyote-European wolf-Maned wolf-Red fox	13,241.23	18.21	14.44
Dog-Coyote-European wolf-Maned wolf-Red fox-Tiger	42,150.48	65.83	45.95

fossil Carnivora. Combining these approaches with the rapidly evolving toolkit of machine learning and artificial intelligence holds great promise for the future of paleoneurology and its ability to shed light on the evolutionary history of nervous systems.

Author Contributions

Study concept and design: Muhammad A. Spocter. Collection of and qualitative analysis of data: Emily Baer, Phuoc D. Nguyen, Stefan Lilly, Jiyoon Song, Mathew Yee, Rogier B. Mars, Olivia Matz, Rachna Sahasrabudhe, Douglas R. Hall, Susan La, Peter F. Cook, Brandon J. Merritt, Pallavi Mahesh, Christelle Eliacin, Kathleen Bitterman, Rachel Dunn, and Muhammad A. Spocter. Statistical analysis and interpretation: Patrick R. Hof, Paul R. Manger, Rachel Dunn, Chet C. Sherwood, and Muhammad A. Spocter. Procurement, preparation, and fixation of tissue: Mads F. Bertelsen, Peter F. Cook, Rachel Dunn, Rogier B. Mars, Cheuk Y. Tang, Chet C. Sherwood, Kathleen Bitterman, Paul R. Manger, and Muhammad A. Spocter. Obtained funding: Muhammad A. Spocter and Paul R. Manger. Drafting of the manuscript: Muhammad A. Spocter, Patrick R. Hof, Paul R. Manger, and Chet C. Sherwood. Photomicrography and preparation of figures and tables: Rachel Dunn, Kathleen Bitterman, and Muhammad A. Spocter. Critical revision of the manuscript for important intellectual content: Muhammad A. Spocter, Rachel Dunn, Paul R. Manger, Chet C. Sherwood, and Patrick R. Hof. Study supervision: Muhammad A. Spocter, Rachel Dunn, and Kathleen Bitterman.

Acknowledgments

We are grateful for the assistance given by Dr. Ian Glidden in scanning select fossil specimens and would also like to extend a special thanks to Dr. Adrienne Stroup and the Field Museum of Natural History for loaning us the endocast specimens to complete this study. We are also grateful for our community partnership with the Des Moines School District (Central Campus) which has helped to foster interest in STEM fields through supporting high school student involvement in our research.

Ethics Statement

For detailed information on relevant ethical standards and criteria, please refer to the Imaging subsection under Methods.

Conflicts of Interest

The authors declare no conflicts of interest.

Data Availability Statement

All quantitative data have been included in the manuscript and imaging data can be provided upon request.

Peer Review

The peer review history for this article is available at https://publons.com/publon/10.1002/cne.70014

References

Barton, R. A. 2001. "The Coordinated Structure of Mosaic Brain Evolution." *Behavioral and Brain Sciences* 24: 281–282.

Barton, R. A., and P. H. Harvey. 2000. "Mosaic Evolution of Brain Structure in Mammals." *Nature* 405: 1055–1058.

Beaudet, A., and E. Gilissen. 2018. "Fossil Primate Endocasts: Perspectives From Advanced Imaging Techniques." In *Digital Endocasts: From Skulls to Brains*, edited by E. Bruner, N. Ogihara, and H. Tanabe, 47–58. Nagoya: Springer.

Behrens, T. E., H. J. Berg, S. Jbabdi, M. F. Rushworth, and M. W. Woolrich. 2007. "Probabilistic Diffusion Tractography with Multiple Fibre Orientations: What can we Gain?." *NeuroImage* 34, no. 1: 144–155.

Benson-Amram, S., B. Dantzer, G. Stricker, E. M. Swanson, and K. E. Holekamp. 2016. "Brain Size Predicts Problem-Solving Ability in Mammalian Carnivores." *Proceedings of the National Academy of Sciences* 113: 2532–2537.

Bininda-Emonds, O. R., M. Cardillo, K. E. Jones, et al. 2007. "The Delayed Rise of Present-Day Mammals." *Nature* 446, no. 7135: 507–512.

Blinkov, S. M., and I. I. Glezer. 1968. *The Human Brain in Figures and Tables: A Quantitative Handbook*. New York: Plenum Press.

Boch, M., K. Karadachka, K. Kee Loh, et al. 2024. "Comparative Neuroimaging of the Carnivoran Brain: Cortical Sulci." *eLife* 13: RP100851.

Borne, L., D. Rivière, M. Mancip, and J. F. Manging. 2020. "Automatic Labeling of Cortical Sulci Using Patch- or CNN-Based Segmentation Techniques Combined With Bottom-Up Geometric Constraints." *Medical Image Analysis* 62: 101651.

Bruner, E., N. Ogihara, and H. C. Tanabe. 2018. *Digital Endocasts*. Tokyo: Springer.

Bush, E. C., and J. M. Allman. 2004. "The Scaling of Frontal Cortex in Primates and Carnivores." *PNAS* 101, no. 11: 3962–3966.

Chengetanai, S., J. D. Tenley, M. F. Bertelsen, et al. 2020. "Brain of the African Wild Dog. I. Anatomy, Architecture, and Volumetrics." *Journal of Comparative Neurology* 528, no. 18: 3245–3261.

Dumoncel, J., G. Subsol, S. Durrleman, et al. 2021. "Are Endocasts Reliable Proxies for Brains? A 3D Quantitative Comparison of the Extant Human Brain and Endocast." *Journal of Anatomy* 238, no. 2: 480–488.

Finarelli, J. A., and J. J. Flynn. 2009. "Brain-Size Evolution and Sociality in Carnivora." *Proceedings of the National Academy of Sciences of the United States of America* 106, no. 23: 9345–9349.

Finlay, B. L., and R. B. Darlington. 1995. "Linked Regularities in the Development and Evolution of Mammalian Brains." *Science* 268: 1578–1584.

Finlay, B. L., R. B. Darlington, and N. Nicastro. 2001. "Developmental Structure in Brain Evolution." *Behavioral and Brain Sciences* 24: 263–278.

Foster, M., S. Dwibhashyam, D. Patel, et al. 2024. "Comparative Anatomy of the Caudate Nucleus in Canids and Felids: Associations With Brain Size, Curvature, Cross-Sectional Properties, and Behavioral Ecology." *Journal of Comparative Neurology* 532, no. 5: e25618. https://doi.org/10.1002/cne.25618.

Foubet, O., J. F. Mangin, Z. Y. Sun, C. C. Sherwood, and W. D. Hopkins. 2024. "Phylogenetic Differences in the Morphology and Shape of the Central Sulcus in Great Apes and Humans: Implications for the Evolution of Motor Functions." *Cerebral Cortex (New York, N.Y.: 1991)* 34, no. 6: bhae232.

Goedhart, J., and M. Rishniw. 2021. "BA- plotteR —A Web Tool for Generating Bland–Altman Plots and Constructing Limits of Agreement." *Research in Veterinary Science* 137: 281–286.

Grewal, J. S., T. Gloe, J. Hegedus, et al. 2020. "Brain Gyrification in Wild and Domestic Canids: Has Domestication Changed the Gyrification Index in Domestic Dogs?." *Journal of Comparative Neurology* 528, no. 18: 3209–3228.

Hassanin, A., G. Veron, A. Ropiquet, et al. 2021. "Evolutionary History of Carnivora (Mammalia, Laurasiatheria) Inferred From Mitochondrial Genomes." *PLoS ONE* 16, no. 2: e0240770.

Jerison, H. J. 2012. "Digitized Fossil Brains: Neocorticalization." *Biolinguistics* 6: 383–392.

Kharlamova, A. S., S. V. Saveliev, A. V. Protopopov, B. C. Maseko, A. Bhagwandin, and P. R. Manger. 2015. "The Mummified Brain of a Pleistocene Woolly Mammoth (*Mammuthus primigenius*) Compared With the Brain of the Extant African Elephant (*Loxodonta africana*)." *Journal of Comparative Neurology* 523: 2326–2343.

Labra, N., A. Mounier, Y. Leprince, et al. 2024. "What Do Brain Endocasts Tell Us? A Comparative Analysis of the Accuracy of Sulcal Identification by Experts and Perspectives in Palaeoanthropology." *Journal of Anatomy* 244, no. 2: 274–296.

Law, C. J., G. J. Slater, and R. S. Mehta. 2018. "Lineage Diversity and Size Disparity in Musteloidea: Testing Patterns of Adaptive Radiation Using Molecular and Fossil-Based Methods." *Systematic Biology* 67: 127–144.

Lyras, G. A. 2009. "The Evolution of the Brain in Canidae (Mammalia: Carnivora)." *Scripta Geologica* 139: 1–93.

Lyras, G. A., A. Giannakopoulou, M. Kouvari, and G. C. Papadopoulos. 2016. "Evolution of Gyrification in Carnivores." *Brain, Behavior and Evolution* 88, no. 3–4: 187–203.

Mai, J. K., T. Voss, and G. Paxinos. 2015. *Atlas of the Human Brain*. New York: Academic Press.

Manger, P. R., M. Prowse, M. Haagensen, and J. Hemingway. 2012. "Quantitative Analysis of Neocortical Gyrencephaly in African Elephants (*Loxodonta africana*) and Six Species of Cetaceans: Comparison With Other Mammals." *Journal of Comparative Neurology* 520, no. 11: 2430–2439.

Manger, P. R., M. A. Spocter, and N. Patzke. 2013. "The Evolutions of Large Brain Size in Mammals: The 'Over-700-Gram Club Quartet'." *Brain, Behavior and Evolution* 82, no. 1: 68–78.

Mettler, F. A. 1956. *Culture and the Structural Evolution of the Neural System. James Arthur Lecture on the Evolution of the Human Brain*. New York: American Museum Natural History.

Michaud, M., S. L. D. Toussaint, and E. Gilissen. 2022. "The Impact of Environmental Factors on the Evolution of Brain Size in Carnivorans." *Communications Biology* 5, no. 1: 998.

Mitchell, J. S. 2015. "Extant-Only Comparative Methods Fail to Recover the Disparity Preserved in the Bird Fossil Record." *Evolution; International Journal of Organic Evolution* 69, no. 9: 2414–2424.

Nelson, J., E. M. Woeste, K. Oba, et al. 2024. "Neuropil Variation in the Prefrontal, Motor, and Visual Cortex of Six Felids." *Brain Behavior and Evolution* 99, no. 1: 25–44. https://doi.org/10.1159/000537843.

Nguyen, V. T., R. Uchida, A. Warling, et al. 2020. "Comparative Neocortical Neuromorphology in Felids: African Lion, African Leopard, and Cheetah." *Journal of Comparative Neurology* 528, no. 8: 1392–1422.

Nyakatura, K., and O. R. Bininda-Emonds. 2012. "Updating the Evolutionary History of Carnivora (Mammalia): A New Species-Level Supertree Complete With Divergence Time Estimates." *BMC Biology* 10: 1–31.

Oddes, D., A. Ngwenya, I. B. Malungo, et al. 2023. "Orexinergic Neurons in the Hypothalami of an Asiatic Lion, an African Lion, and a Southeast African Cheetah." *Journal of Comparative Neurology* 531, no. 3: 366–389.

Orme, D., R. Freckleton, G. Thomas, et al. 2018. *Caper: Comparative Analyses of Phylogenetics and Evolution in R*. R package Version 0.4. http://CRAN.R-project.org/package=caper.

Palazzi, X. 2011. *The Beagle Brain in Stereotaxic Coordinates*. New York: Springer.

Perri, A. R., K. J. Mitchell, A. Mouton, et al. 2021. "Dire Wolves Were the Last of an Ancient New World Canid Lineage." *Nature* 591: 87–91.

Racicot, K. J., J. R. Ham, J. K. Augustine, R. Henriksen, D. Wright, and A. N. Iwaniuk. 2024. "A Comparison of Telencephalon Composition Among Chickens, Junglefowl, and Wild Galliforms." *Brain, Behavior and Evolution* 99, no. 1: 13–24.

Radinsky, L. B. 1973. "Evolution of the Canid Brain." *Brain Behavior and Evolution* 7: 169–202.

Radinsky, L. B. 1975. "Evolution of the Felid Brain." *Brain Behavior and Evolution* 11: 214–254.

Reep, R. L., B. L. Finlay, and R. B. Darlington. 2007. "The Limbic System in Mammalian Brain Evolution." *Brain, Behavior and Evolution* 70, no. 1: 57–70.

Reep, R. L., J. I. Johnson, R. C. Switzer, and W. I. Welker. 1989. "Manatee Cerebral Cortex: Cytoarchitecture of the Frontal Region in *Trichechus manatus Latirostris*." *Brain Behavior and Evolution* 34: 365–386.

Rehkamper, G., H. D. Frahm, and K. Zilles. 1991. "Quantitative Development of Brain and Brain Structures in Birds (Galliformes and Passeriformes) Compared to That in Mammals (Insectivores and Primates)." *Brain Behavior and Evolution* 37: 125–143.

Rogers, J., P. Kochunov, K. Zilles, et al. 2010. "On the Genetic Architecture of Cortical Folding and Brain Volume in Primates." *Neuroimage* 53, no. 3: 1103–1108.

Sacco, J. C., E. Starr, A. Weaver, R. Dietz, and M. A. Spocter. 2023. "Resequencing of the TMF-1 (TATA Element Modulatory Factor) Regulated

Protein (TRNP1) Gene in Domestic and Wild Canids." *Canine Medicine and Genetics* 10, no. 1: 10.

Sakai, S. T., B. M. Arsznov, B. L. Lundrigan, and K. E. Holekamp. 2011. "Virtual Endocasts: An Application of Computed Tomography in the Study of Brain Variation Among Hyenas." *Annals of the New York Academy of Sciences* 1225, no. Suppl. 1: E160–E170.

Sakai, S. T., B. M. Arsznov, A. E. Hristova, E. J. Yoon, and B. L. Lundrigan. 2016. "Big Cat Coalitions: A Comparative Analysis of Regional Brain Volumes in Felidae." *Frontiers in Neuroanatomy* 10: 99.

Scott, G. H. 1963. "Uniformitarianism, the Uniformity of Nature, and Paleoecology." *New Zealand Journal of Geology and Geophysics* 6, no. 4: 510–527.

Slater, G. J., L. J. Harmon, and M. E. Alfaro. 2012. "Integrating Fossils With Molecular Phylogenies Improves Inference of Trait Evolution." *Evolution; International Journal of Organic Evolution* 66: 3931–3944.

Slizewski, A., M. Friess, and P. Semal. 2010. "Surface Scanning of Anthropological Specimens: Nominal-Actual Comparison With Low-Cost Laser Scanner and High-End Fringe Light Projection Surface Scanning Systems." *Quartär* 57: 179–187.

Smaers, J. B., R. S. Rothman, D. R. Hudson, et al. 2021. "The Evolution of Mammalian Brain Size." *Science Advances* 7: eabe2101. https://doi.org/10.1126/sciadv.abe2101.

Smaers, J. B., C. S. Mongle, and A. Kandler. 2016. "A Multiple Variance Brownian Motion Framework for Estimating Variable Rates and Inferring Ancestral States." *Biological Journal of the Linnean Society* 118, no. 1: 78–94.

Smith, R. J. 1993. "Bias in Equations Used to Estimate Fossil Primate Body Mass." *Journal of Human Evolution* 25: 31–41.

Solé, F., T. Smith, E. D. Bast, V. A. Codrea, and E. Gheerbrant. 2016. "New Carnivoraforms from the Latest Paleocene of Europe and Their Bearing on the Origin and Radiation of Carnivoraformes (Carnivoramorpha, Mammalia)." *Journal of Vertebrate Paleontology* 36, no. 2.

Spaulding, M., and J. J. Flynn. 2012. "Phylogeny of the Carnivoramorpha: The Impact of Postcranial Characters." *Journal of Systematic Palaeontology* 10: 653–677.

Spocter, M. A., A. Uddin, J. C. Ng, et al. 2018. "Scaling of the Corpus Callosum in Wild and Domestic Canids: Insights Into the Domesticated Brain." *Journal of Comparative Neurology* 526, no. 15: 2341–2359.

Spocter, M. A., and P. R. Manger. 2007. "The use of Cranial Variables for the Estimation of Body Mass in Fossil Hominins." *American Journal of Physical Anthropology* 134, no. 1: 92–105.

Stephan, H. 1960. "Methodische Studien über den Quantitativen Vergleich Architektonischer Struktureinheiten des Gehirns." *Zeitschrift für wissenschaftliche Zoologie* 164: 143–172.

Stephan, H., H. Frahm, and G. Baron. 1981. "New and Revised Data on Volumes of Brain Structures in Insectivores and Primates." *Folia Primatology* 35: 1–29.

Tedford, R. H., X. Wang, and B. E. Taylor. 2009. "Phylogenetic Systematics of the North American Fossil Caninae (Carnivora: Canidae)." *Bulletin of the American Museum of Natural History* 325: 1–218.

Tobias, P. V. 1994. "The Craniocerebral Interface in Early Hominids." In *Integrative Paths to the Past, Paleoanthropological Advances in Honor of F. Clark Howell*, edited by R. S Corruccini and R. L. Ciochon, 185–204. Englewood Cliffs, NJ: Prentice Hall.

Warton, D. I., R. A. Duursma, D. S. Falster, and S Taskinen. 2011. "Smart—An R Package for Estimation and Inference About Allometric Lines." *Methods in Ecology and Evolution* 3, no. 2: 257–259.

Welker, W. I., J. I. Johnson, and A. Noe. 2006. *Comparative Mammalian Brain Collections*. Washington, DC: Worldwide Web. http://brainmuseum.org/index.html.

Werdelin, L., N. Yamaguchi, W. E. Johnson, and S. J. O-Brien. 2010. "Phylogeny and Evolution of Cats (Felidae)." In *The Biology and Conservation of Wild Felids*, edited by D. M. Macdonald and A. Loveridge, 59–82. Oxford: Oxford University Press.

Yin, D., F. E. Valles, M. S. Fiandaca, et al. 2009. "Striatal Volume Differences Between Non-Human and Human Primates." *Journal of Neuroscience Methods* 176, no. 2: 200–205.

Yopak, K. E., T. J. Lisney, R. B. Darlington, S. P. Collin, J. C. Montgomery, and B. L. Finlay. 2010. "A Conserved Pattern of Brain Scaling From Sharks to Primates." *Proceedings of the National Academy of Sciences of the United States of America* 107, no. 29: 12946–12951.

Yushkevich, P. A., J. Piven, H. C. Hazlett, et al. 2006. "User-Guided 3D Active Contour Segmentation of Anatomical Structures: Significantly Improved Efficiency and Reliability." *Neuroimage* 31, no. 3: 1116–1128.

Zhou, Q., E. Grinspun, D. Zorin, and A Jacobson. 2016. "Mesh Arrangements for Solid Geometry." *ACM Transactions on Graphics* 35, no. 4: 1–15.